

Article

# Jahn–Teller Magnets

Alexander Moskvina<sup>1,2</sup> 

<sup>1</sup> Department of Theoretical Physics, Ural Federal University, 620083 Ekaterinburg, Russia; alexander.moskvina@urfu.ru

<sup>2</sup> Institute of Metal Physics Ural Branch of the Russian Academy of Sciences, 620108 Ekaterinburg, Russia

**Abstract:** A wide class of materials with different crystal and electronic structures including quasi-2D unconventional superconductors, such as cuprates, nickelates, ferropnictides/chalcogenides, ruthenate  $\text{Sr}_2\text{RuO}_4$ , and 3D systems, such as manganites  $\text{RMnO}_3$ , ferrates  $(\text{CaSr})\text{FeO}_3$ , nickelates  $\text{RNiO}_3$ , silver oxide  $\text{AgO}$ , are based on Jahn–Teller  $3d$  and  $4d$  ions. These unusual materials, called Jahn–Teller (JT) magnets, are characterized by an extremely rich variety of phase states, spanning from non-magnetic and magnetic insulators to unusual metallic and superconducting states. The unconventional properties of JT magnets can be attributed to the instability of their highly symmetric Jahn–Teller “progenitors” with the ground orbital  $E$ -state with respect to charge transfer, anti-Jahn–Teller  $d$ - $d$  disproportionation, and the formation of a system of effective local composite spin–singlet or spin–triplet, electronic, or hole  $S$ -type bosons moving in a non-magnetic or magnetic lattice. We consider specific features of the anti-JT-disproportionation reaction, properties of the electron–hole dimers, possible phase states and effective Hamiltonians for single- and two-band JT magnets, concluding with a short overview of physical properties for actual JT magnets.

**Keywords:** Jahn–Teller magnets; anti-JT disproportionation; spin–singlet and spin–triplet composite bosons; phase states

## 1. Introduction

We refer to compounds based on Jahn–Teller  $3d$ - and  $4d$ -ions [1–4] with configurations of the  $t_{2g}^{n_1} e_g^{n_2}$  type in a highly symmetrical octahedral, cubic, or tetrahedral environment, and with a ground state orbital  $E$ -doublet, as Jahn–Teller (JT) magnets. These are compounds based on tetra complexes with the configuration  $d^1$  ( $\text{Ti}^{3+}$ ,  $\text{V}^{4+}$ ), low-spin (LS) configuration  $d^3$  ( $\text{V}^{2+}$ ,  $\text{Cr}^{3+}$ ,  $\text{Mn}^{4+}$ ), and high-spin (HS) configuration  $d^6$  ( $\text{Fe}^{2+}$ ,  $\text{Co}^{3+}$ ); they also include octa complexes with HS configuration  $d^4$  ( $\text{Cr}^{2+}$ ,  $\text{Mn}^{3+}$ ,  $\text{Fe}^{4+}$ ,  $\text{Ru}^{4+}$ ), low-spin configuration  $d^7$  ( $\text{Co}^{2+}$ ,  $\text{Ni}^{3+}$ ,  $\text{Pd}^{3+}$ ), as well as octa complexes with configuration  $d^9$  ( $\text{Cu}^{2+}$ ,  $\text{Ni}^{1+}$ , and  $\text{Ag}^{2+}$ ) (see Table 1). The term “Jahn–Teller magnets”, referring to compounds that contain Jahn–Teller ions, was introduced more than 40 years ago in a well-known article by Russian scientists Kugel and Khomskii (Uspekhi fizicheskikh nauk, 136, 621 (1982), in Russian), although in the translated version (see Ref. [2]) the term “Jahn–Teller magnetic materials” was used with a focus on 3d magnetic insulators with a cooperative Jahn–Teller effect. However, the class of JT magnets extends much further than the materials considered by Kugel and Khomskii [2]. It includes a large number of promising materials that are at the forefront of modern condensed matter physics, including manganites  $\text{RMnO}_3$ , ferrates  $(\text{Ca,Sr})\text{FeO}_3$ , ruthenates  $\text{RuO}_2$ ,  $(\text{Ca,Sr})\text{RuO}_3$ ,  $(\text{Ca,Sr})_2\text{RuO}_4$ , a wide range of ferropnictides ( $\text{FePn}$ ) and ferrochalcogenides ( $\text{FeCh}$ ), 3D nickelates  $\text{RNiO}_3$ , 3D-cuprates  $\text{KCuF}_3$ , 2D cuprates  $(\text{La}_2\text{CuO}_4, \dots)$  and nickelates  $\text{RNiO}_2$ , and silver-based compounds ( $\text{AgO}$ ,  $\text{AgF}_2$ ) (see Table 1). Among these materials, it is necessary to highlight JT magnets experiencing charge transfer, particularly disproportionation, as they exhibit a rich spectrum of unique properties, ranging from varied types of magnetic and charge ordering to metal–insulator transitions and superconductivity. Interestingly, the selection of cuprates as potential superconducting materials and the discovery of high-temperature superconductivity (HTSC) [5]



**Citation:** Moskvina, A. Jahn–Teller Magnets. *Magnetochemistry* **2023**, *9*, 224. <https://doi.org/10.3390/magnetochemistry9110224>

Academic Editors: Carlos J. Gómez García and Boris Tsukerblat

Received: 29 May 2023

Revised: 19 September 2023

Accepted: 27 September 2023

Published: 2 November 2023



**Copyright:** © 2023 by the author. Licensee MDPI, Basel, Switzerland. This article is an open access article distributed under the terms and conditions of the Creative Commons Attribution (CC BY) license (<https://creativecommons.org/licenses/by/4.0/>).

were influenced by the outstanding Jahn–Teller character of  $\text{Cu}^{2+}$  ions [1]. Attempts to explain the HTSC of cuprates led to the development and dissemination of ideas about the disproportionation. Many authors considered disproportionation as a mechanism (“negative- $U$ ” model) leading to the “glueless” superconductivity of a system of local electron pairs, or composite bosons (see, e.g., Refs. [6–23]). The concept of superconductivity, understood as a Bose–Einstein condensation (BEC) of local composite bosons (two electrons bound in real space), was introduced by Ogg Jr. in 1946 [24] and developed by Schafroth in 1954–55 [25]. However, due to the triumph of the BCS (Bardeen–Cooper–Schrieffer) theory, the notions of local composite bosons and preformed pairs were practically forgotten for many years. The discovery of HTSC cuprates in 1986 revived interest in the idea of local pairing [26], especially since this idea has been supported by K. A. Mueller, the discoverer of HTSC [27]. Currently, there is convincing experimental evidence that the local pairing of carriers takes place well above  $T_c$ , at least in underdoped cuprates [28]. At the same time, to date, the HTSC theory has been dominated by approaches based on the BCS paradigm, i.e., on the representations of the BCS model theory applicable to the description of typical low-temperature superconductors. This is largely due to the fact that an appealingly straightforward picture of preformed pairs and BEC superconductivity in cuprates seemingly came to be at odds with several experimental observations, indicative of typical Fermi liquid behavior; notably, with indications of a well-defined Fermi surface (FS) in, at least, overdoped cuprates, the thermal and electrical conductivity were found to follow the standard Wiedemann–Franz law. Quantum oscillations have been observed as well in various cuprates [29].

**Table 1.**  $3d^n$  and  $4d^n$  JT magnets. See the text for references and details.

JT Configuration JT Ions	Symm.	LS/HS	Local Boson	Lattice	Representative Compounds
$3d^1(e_g^1):^2E$ $\text{Ti}^{3+}, \text{V}^{4+}, \text{Cr}^{5+}$	tetra	-	$e_g^2: ^3A_{2g}$ $s = 1$	$A_{1g}$ $S = 0$	$\beta\text{-Sr}_2\text{VO}_4$ $(\text{Sr}, \text{Ba})_3\text{Cr}_2\text{O}_8$
$3d^3(e_g^3):^2E$ $\text{V}^{2+}, \text{Cr}^{3+}, \text{Mn}^{4+}$	tetra	LS	$e_g^2: ^3A_{2g}$ $s = 1$	$A_{1g}$ $S = 0$	$\text{Ba}_2\text{VGe}_2\text{O}_7$ (?)
$3d^4(t_{2g}^3 e_g^1):^5E$ $\text{Cr}^{2+}, \text{Mn}^{3+}, \text{Fe}^{4+}$	octa	HS	$e_g^2: ^3A_{2g}$ $s = 1$	$A_{2g}$ $S = 3/2$	$\text{CrO}, \text{CrF}_2$ $\text{Sr}_2\text{FeO}_4$ $(\text{Ca}, \text{Sr}, \text{Ba})\text{FeO}_3$ $(\text{Ca}, \text{Sr}, \text{Ba})_3\text{Fe}_2\text{O}_7$ $\text{RMnO}_3, \text{LaMn}_7\text{O}_{12}$
$4d^4(t_{2g}^3 e_g^1):^5E$ $\text{Ru}^{4+}$	octa	HS	$e_g^2: ^3A_{2g}$ $s = 1$	$A_{2g}$ $S = 3/2$	$(\text{Ca}, \text{Sr})_2\text{RuO}_4$ $(\text{Ca}, \text{Sr})\text{RuO}_3, \text{RuO}_2$ $(\text{Ca}, \text{Sr})_3\text{Ru}_2\text{O}_7$
$3d^6(e_g^3 t_{2g}^3):^5E$ $\text{Fe}^{2+}, \text{Co}^{3+}$	tetra	HS	$e_g^2: ^3A_{2g}$ $s = 1$	$A_{2g}$ $S = 3/2$	$\text{FePn}, \text{FeCh}, \text{Na}_5\text{CoO}_4$
$3d^7(t_{2g}^6 e_g^1):^2E$ $\text{Co}^{2+}, \text{Ni}^{3+}$	octa	LS	$e_g^2: ^3A_{2g}$ $s = 1$	$A_{1g}$ $S = 0$	$\text{RNiO}_3$ $(\text{Li}, \text{Na}, \text{Ag})\text{NiO}_2$
$3d^9(t_{2g}^6 e_g^3):^2E$ $\text{Cu}^{2+}, \text{Ni}^+$	octa	-	$e_g^2: ^3A_{2g}$ $s = 1$	$A_{1g}$ $S = 0$	$\text{CuF}_2, \text{KCuF}_3, \text{K}_2\text{CuF}_4$
$4d^9(t_{2g}^6 e_g^3):^2E$ $\text{Pd}^+, \text{Ag}^{2+}$	octa	-	$e_g^2: ^3A_{2g}$ $s = 1$	$A_{1g}$ $S = 0$	$\text{AgO} (\text{Ag}^{1+} \text{Ag}^{3+} \text{O}_2)$
$3d^9(t_{2g}^6 e_g^3):^2B_{1g}$ $\text{Cu}^{2+}, \text{Ni}^+$	octa* square	-	$t_{1g}^2: ^1A_{1g}$ $s = 0$	$A_{1g}$ $S = 0$	HTSC cuprates $\text{RNiO}_2, \text{CuO}$
$4d^9(t_{2g}^6 e_g^3):^2B_{1g}$ $\text{Pd}^+, \text{Ag}^{2+}$	octa* square	-	$t_{1g}^2: ^1A_{1g}$ $s = 0$	$A_{1g}$ $S = 0$	$\text{AgF}_2, \text{KAgF}_3$ $\text{Cs}_2\text{AgF}_4, \text{LaPdO}_2$ (?)

However, this contradictory behavior can be easily explained if we take into account the possibility of separating the superconducting BEC phase and the normal Fermi liquid phase. Indeed, recently, Pelc et al. [30] introduced a phenomenological model of “local phase separation”, in which two electronic subsystems coexist within the unit cell: itinerant and localized holes. In this model, the  $p$  holes introduced via doping are always itinerant, while the pairing is associated with the localized holes. In fact, they argue that the Fermi liquid subsystem in cuprates is responsible for the normal state with angle-resolved photoemission spectra (ARPES), magnetic quantum oscillations, and Fermi arcs, but not for the unconventional superconducting state. In other words, *cuprate superconductivity is not related to the doped hole pairing*, the carriers that exhibit the Fermi liquid behavior are not the ones that give rise to superconductivity. However, the authors could not elucidate the nature of local pairing to be a central point of the cuprate puzzle.

The disproportionation scenario, which is especially popular in the “chemical” community (“chemical” way to superconductivity), has been addressed earlier by many authors; however, it was not properly developed theoretically. Perhaps that is why it has not yet been a worthy competitor to the traditional BCS approach.

Previously, we proposed a mechanism for “anti-Jahn-Teller disproportionation” in 3d JT magnets [31], which, by analogy with other anti-JT effects [32–34], leads to the removal of orbital degeneracy in JT magnets. As a result, we arrived at the formation of a system of electron and hole centers with orbitally nondegenerate ground states, equivalent to a system of effective local composite spin-triplet bosons moving in a magnetic or nonmagnetic lattice. This mechanism indicated an unconventional bosonic spin-triplet superconductivity in 3d JT magnets, particularly in ferropnictides and ferrochalcogenides, which was predicted back in 2008 [35]. In the past years, new results have been obtained in the study of JT magnets based on both 3d and 4d ions, as well as new arguments both for and against spin-triplet superconductivity.

In this paper, we expand a model of “anti-Jahn-Teller” disproportionation to encompass a wider class of Jahn-Teller magnets, including 4d magnets (ruthenates, silver compounds), and 2D nickelates  $RNiO_2$ , showing that they can all be described within a single scenario. In Section 2, we present a more detailed description of the anti-JT disproportionation for JT magnets and the formation of effective local composite bosons. In Sections 3 and 4, we consider electron-hole (EH) dimers as specific “disproportionation quanta”, delving into their electron and spin structures. Section 5 provides a brief overview of the possible phase states for JT magnets. Sections 6 and 7 present the effective Hamiltonians of single- and two-band JT magnets, providing a brief overview of the properties of real JT magnets. A brief summary is presented in Section 8.

## 2. Anti-Jahn-Teller Disproportionation

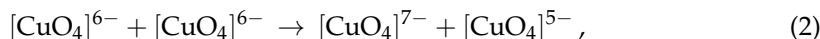
For each JT magnet, one can introduce an imaginary “parent” highly symmetrical phase, or “progenitor”, with a highly symmetrical octahedral, tetrahedral, or cubic environment of the JT ion. The lifting of the orbital  $E$ -degeneracy in the high-symmetry “progenitor” JT magnets can be associated with the specifics of the crystal structure, for example, in “apex-free” 2D cuprates ( $Nd_2CuO_4$ ) and  $RNiO_2$  nickelates, and with the conventional Jahn-Teller effect [1,2], which, as a rule, leads to the formation of a low-symmetry insulating antiferromagnetic ( $La_2CuO_4$ ,  $KCuF_3$ ,  $LaMnO_3$ ) or ferromagnetic ( $K_2CuF_4$ ) phase. A competing mechanism for removing orbital degeneracy in the aforementioned JT magnets is the “anti-Jahn-Teller”, “symmetric”  $d$ - $d$ -disproportionation, illustrated by the following scheme:



assuming the formation of a system of bound or relatively free electronic  $d^{n+1}$  and hole  $d^{n-1}$  centers, differing by a pair of electrons/holes. Formally, an electron/hole center can be represented as a hole/electron center with a pair of electrons/holes  $d^2/\underline{d}^2$  localized at the center. In other words, a disproportionate system can be formally represented as a system of effective local spin-singlet or spin-triplet composite electron/hole bosons

“moving” in the lattices of hole/electron centers. Note that in the frames of the toy model (1), the disproportionation energy  $\Delta_{dd}$  formally coincides with the energies of local correlations  $U_{dd}$ , giving a reason to associate symmetric  $d$ - $d$ -disproportionation with the negative- $U$  phenomenon.

Obviously, in systems with strong  $d$ - $p$ -hybridization (cation–anion covalency), the disproportionation reaction (1) must be written in a “cluster” language, for example, for  $\text{CuO}_4$  clusters in the  $\text{CuO}_2$  cuprate planes:



instead of

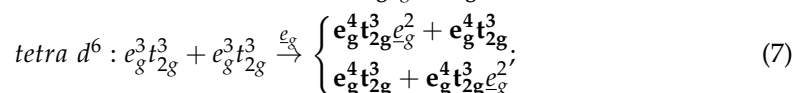
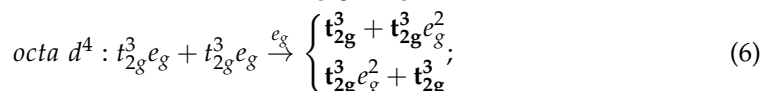
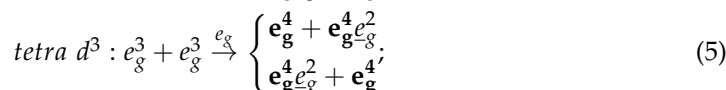
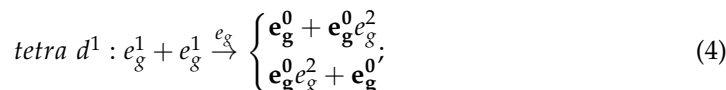


The cation–ligand cluster representations of the  $d^n, d^{n\pm 1}$ -centers immediately show the important role of the bond-stretching, or so-called “breathing mode” of the ligand displacements in perovskite-type JT magnets with corner-shared coupling of neighboring octahedral  $d$ -centers. The displacement amplitude of the common ligand for two centers during disproportionation can reach values greater than of 0.1 Å due to the large difference in the cation–ligand separation for the electron and hole centers. Thus, the Cu–O separation for  $\text{CuO}_4$  centers in cuprates increases by 0.2 Å from the hole  $[\text{CuO}_4]^{5-}$  to electron  $[\text{CuO}_4]^{7-}$  center [36].

The bond-stretching, or breathing-type distortion of metal–oxygen clusters, is a clear fingerprint of a static charge disproportionation observed in JT magnets, such as 3D nickelates and ferrates (see, e.g., Refs. [37,38]), while the softening and broadening of the bond stretching phonon mode observed in JT magnets, such as HTSC cuprates (LSCO, YBCO, Hg1201) and manganites  $\text{LaMnO}_3$  [39], is believed to be an indication of the dynamical disproportionation. Note that the electron–lattice interaction leads to the stability of the electron and hole centers in the lattice of the parent system with the ground states of all three centers—the electron, parent, and hole—corresponding to different values of the local breathing configuration coordinates  $Q_{A_{1g}}$ :  $+Q_0, 0, -Q_0$ , respectively.

Symmetric  $d$ - $d$ -disproportionation, in contrast to “asymmetric”, “single-center”,  $d$ - $p$ -disproportionation [40–42], has a two-center character, although it may include  $d$ - $p$ -transfer between clusters. Obviously, symmetric  $d$ - $d$  disproportionation will be energetically more favorable in progenitor Mott–Hubbard JT magnets, and vice versa, asymmetric  $d$ - $p$ -disproportionation will be more energetically favorable in charge-transfer (CT) insulators (“negative charge transfer” materials).

It is worth noting that all the JT magnets are characterized by empty, half-filled, or fully filled  $t_{2g}$  subshells with orbitally non-degenerate  $A_{1g}, A_{2g}$ , or  $S$ -type ground states, and with only one  $e_g$  electron or hole [3,4]. Obviously, the low-energy anti-JT-disproportionation implies the  $e_g$ - $e_g$  intersite transfer with the formation of the empty, half-filled, or fully filled  $e_g$  subshells with the  $S$ -type ground state for the electron and hole centers. In all cases, we arrive at relatively stable  $S$ -type configurations of electron and hole centers. For all JT magnets, the anti-JT disproportionation reactions can be written as follows:



$$\text{octa } d^7 : t_{2g}^6 e_g + t_{2g}^6 e_g \xrightarrow{e_g} \begin{cases} \mathbf{t}_{2g}^6 + \mathbf{t}_{2g}^6 e_g^2; \\ \mathbf{t}_{2g}^6 e_g^2 + \mathbf{t}_{2g}^6; \end{cases} \quad (8)$$

$$\text{octa } d^9 : t_{2g}^6 e_g^3 + t_{2g}^6 e_g^3 \xrightarrow{e_g} \begin{cases} \mathbf{t}_{2g}^6 e_g^4 e_g^2 + \mathbf{t}_{2g}^6 e_g^4 \\ \mathbf{t}_{2g}^6 e_g^4 + \mathbf{t}_{2g}^6 e_g^4 e_g^2. \end{cases} \quad (9)$$

In Equations (4)–(9), we singled out both the composite boson and (bold) stable basic configurations of the electron and hole centers. Obviously, for JT magnets with on-site progenitor configurations of  $e_g^1$ ,  $t_{2g}^3 e_g^1$ ,  $t_{2g}^6 e_g^1$ , we are dealing with the transfer of the  $e_g$  electron, while for configurations of  $e_g^3 t_{2g}^3$  and  $t_{2g}^6 e_g^3$ , it is correct to speak of the  $e_g$  hole ( $\bar{e}_g$ ) transfer. Thus, for these configurations, we arrive at the doublet of ionic states with site-centered charge orders, or two centers that differ in the transfer (exchange) of two  $e_g$  electrons or two  $e_g$  holes, respectively, which can be thought of as effective local composite bosons. For centers with high (octahedral, tetrahedral) symmetry, these effective bosons will be described by the low-energy  $S$ -type Hund configuration  $e_g^2; ^3A_{2g}$ ; or  $e_g^2; ^3A_{2g}$ . It should be noted that effective bosons cannot be considered conventional quasiparticles, they are an integral part of many-electron configurations [43,44].

All JT magnets can be conditionally classified as “single-band” or “two-band” magnets. In single-band JT magnets with configurations of  $d^1$ ,  $d^3$ ,  $d^7$ , and  $d^9$ , effective electron ( $d^1$ ,  $d^7$ ) or hole ( $d^3$ ,  $d^9$ ) composite bosons move in the lattices of ions with completely filled shells, while in two-band JT magnets ( $d^4$ ,  $d^6$ ), the lattices include ions with half filled  $t_{2g}$  subshells.

The optimal configurations and the spin of the composite boson, along with the orbital state and the local spin of the lattice—which are formed as a result of anti-JT disproportionation in JT magnets with a  $3d^n$  configuration—as well as some  $4d^n$  JT configurations, are presented in the fourth and fifth columns of Table 1. Note that in all cases, the complete disproportionation leads to a system of composite bosons with a concentration of 1/2, indicating half-filling.

### 3. Electron–Hole Dimers

A pair of bound electron and hole centers, or an EH dimer, is a kind of “disproportionation quantum”. In Mott–Hubbard insulators, EH dimers are low-energy metastable charge excitations above the ground state or may be the result of the self-trapping of  $d$ - $d$  CT excitons [45].

The two-electron/hole charge exchange reaction in the EH dimer

$$d_1^{n+1} + d_2^{n-1} \xleftrightarrow{e_g^2; ^3A_{2g}} d_1^{n-1} + d_2^{n+1}, \quad (10)$$

is controlled by the effective local boson transfer integral

$$t_B = \langle d_1^{n+1} d_2^{n-1} | \hat{H}_B | d_1^{n-1} d_2^{n+1} \rangle, \quad (11)$$

where  $\hat{H}_B$  is an effective two-particle (bosonic) transfer Hamiltonian, and we assume ferromagnetic-ordered spins of the two centers. As a result of this quantum process, the bare ionic states with site-centered charge orders and the same bare energy  $E_0$  transform into two EH dimer states with indefinite valence and bond-centered charge order

$$|\pm\rangle = \frac{1}{\sqrt{2}} (|d_1^{n+1} d_2^{n-1}\rangle \pm |d_1^{n-1} d_2^{n+1}\rangle) \quad (12)$$

with energies  $E_{\pm} = E_0 \pm t_B$ . In other words, the exchange reaction restores the bare charge symmetry. In both  $|\pm\rangle$  states, the on-site number of  $d$  electrons is indefinite with quantum fluctuations between  $(n + 1)$  and  $(n - 1)$ , and a mean value  $n$ . Interestingly, in contrast with the ionic states, the EH dimer states  $|\pm\rangle$  have distinct electron–holes and inversion

symmetry, even parity (*s*-type symmetry) for  $|+\rangle$  states, and odd parity (*p*-type symmetry) for  $|-\rangle$  states, respectively. Both states are coupled by a large electric dipole matrix element:

$$\langle +|\hat{\mathbf{d}}|-\rangle = 2e\mathbf{R}_{12}, \quad (13)$$

where  $R_{12}$  is a 1–2 separation. The two-particle transport (10) can be realized through two successive one-particle processes with the  $e_g$  electron transfer as follows:

$$d_1^{n+1} + d_2^{n-1} \xrightarrow{e_g} d_1^n + d_2^n \xrightarrow{e_g} d_1^{n-1} + d_2^{n+1},$$

hence, the two-particle transfer integral  $t_B$  can be evaluated as follows:

$$t_B = -t_{e_g e_g}^2 / U \approx -J_{kin}(e_g e_g), \quad (14)$$

where  $t_{e_g e_g}$  is the one-particle transfer integral for the  $e_g$  electron,  $U$  is the mean transfer energy. It means that the two-particle bosonic transfer integral can be directly coupled with the kinetic  $e_g$ -contribution  $J_{kin}(e_g e_g)$  to the Heisenberg  $e_g$ - $e_g$  exchange integral. Both  $t_B$  and  $J_{kin}(e_g e_g)$  are determined by the second-order one-particle transfer mechanism. It should be noted that a negative sign of the two-particle CT integral  $t_B$  points to the energy stabilization of the *s*-type EH dimer state  $|+\rangle$ .

Moreover, we should emphasize once more that the stabilization of EH dimers is provided by a strong electron–lattice effect with a striking intermediate oxygen atom polarization and displacement concomitant with charge exchange. In a sense, the EH dimer may be a bosonic counterpart of the Zener  $\text{Mn}^{4+}$ - $\text{Mn}^{3+}$  polaron [46]. It is no wonder that even in a generic disproportionated system  $\text{BaBiO}_3$ —instead of simple checkerboard charge orderings of  $\text{Bi}^{3+}$  and  $\text{Bi}^{5+}$  ions—we arrive at a CDW (charge density wave) state with the alteration of expanded  $\text{Bi}^{(4-\rho)+}\text{O}_6$  and compressed  $\text{Bi}^{(4+\rho)+}\text{O}_6$  octahedra with  $0 < \rho \ll 1$  [47]. The enormously large values of oxygen thermal parameters in  $\text{BaBiO}_3$  [48] underscore the great importance of dynamical oxygen breathing modes providing some sort of “disproportionation glue”. A sharp rise in the oxygen thermal parameter in the high-temperature O phase of  $\text{LaMnO}_3$  [49] or in several “competing” phases found by Huang et al. [50], compared to the bare AFI phase, is believed to be a clear signature of the high-temperature manganese disproportionation [51].

We examine an EH dimer as a dynamic–charge–fluctuating bipolaronic system composed of coupled electron  $d^{n+1}$  and hole  $d^{n-1}$  centers that are glued in a lattice, due to a specific local expansion/contraction mode of neighboring clusters (half-breathing or breathing mode), and strong electron–lattice polarization effects.

#### 4. Spin Structure of EH Dimers

Let us address the spin degrees of freedom, which are of great importance for the magnetic properties of EH dimers as nucleation centers for a rich variety of different phases. First, we note that the structures of EH dimers are significantly different in single- and two-band JT magnets. In EH dimers of JT magnets based on  $d^1$ ,  $d^7$ , and  $d^9$  configurations, the spin–triplet boson “moves” along the spinless centers (see Table 1), which leads to a trivial spin structure of the dimer. A more complicated situation is realized for EH dimers of JT magnets based on  $d^4$  and  $d^6$  configurations, where the spin–triplet boson “moves” through the  $d^3(t_{2g}^3)$  centers with spin 3/2 (see Table 1).

The total spin moments of these EH dimers are  $\mathbf{S} = \mathbf{S}_1 + \mathbf{S}_2$ , where  $\mathbf{S}_1$  ( $S_1 = 5/2$ ) and  $\mathbf{S}_2$  ( $S_2 = 3/2$ ) are spins of  $d^5$  and  $d^3$  ( $d^5$  and  $d^3$ ) configurations, respectively, so the total spin magnitudes  $S$  take the values of 1, 2, 3, and 4. In a nonrelativistic approximation, the spin structure of the EH dimer in the bare ionic state  $d^5$ – $d^3$  ( $d^5$ – $d^3$ ) with the site-centered charge order will be determined by isotropic Heisenberg exchange coupling

$$V_{ex} = J(d^5 d^3) (\mathbf{S}_1 \cdot \mathbf{S}_2), \quad (15)$$

with  $J(d^5d^3)$  being a  $d^5-d^3$  ( $d^3-d^5$ ) (super)exchange integral. However, the two site-centered states,  $d^5-d^3$  and  $d^3-d^5$ , are coupled by the two-particle charge transfer characterized by a respective transfer integral, depending on the spin states, as follows:

$$\langle \frac{5}{2} \frac{3}{2}; SM | \hat{H}_B | \frac{3}{2} \frac{5}{2}; SM \rangle = \frac{1}{20} S(S+1) t_B, \quad (16)$$

where  $t_B$  is a spinless transfer integral. Making use of this expression, we can introduce an effective spin operator form for the boson transfer, as follows:

$$\hat{H}_B^{eff} = \frac{t_B}{20} [2(\hat{S}_1 \cdot \hat{S}_2) + S_1(S_1+1) + S_2(S_2+1)], \quad (17)$$

which can be a very instructive tool for qualitative and quantitative analyses of boson transfer effects. Thus, the effective transfer integral of the composite boson strongly depends on the spin state of the electron–hole pair, falling ten-fold as the total spin of the pair changes from  $S = 4$  to  $S = 1$ . In particular, we arrive at a strong, almost two-fold, suppression of the effective transfer integral in the paramagnetic phase, compared with its maximal value  $t_B$  for ferromagnetic ordering ( $S = 4$ ).

Both the conventional Heisenberg exchange coupling  $d^5-d^3$  ( $d^3-d^5$ ) and unconventional two-particle bosonic transfer, or bosonic double exchange, can be easily diagonalized in the total spin  $S$  representation, so that for the energy of the EH dimer, we arrive at

$$E_S = \frac{J(d^5d^3)}{2} [S(S+1) - \frac{25}{2}] \pm \frac{1}{20} S(S+1) t_B, \quad (18)$$

where  $\pm$  corresponds to two quantum superpositions  $|\pm\rangle$  written in a spin representation as follows

$$|SM\rangle_{\pm} = \frac{1}{\sqrt{2}} (|\frac{5}{2} \frac{3}{2}; SM\rangle \pm |\frac{3}{2} \frac{5}{2}; SM\rangle), \quad (19)$$

with  $s$ - and  $p$ -type symmetry, respectively. It is worth noting that the bosonic double exchange contribution formally corresponds to ferromagnetic exchange coupling with  $J_B = -\frac{1}{10}|t_B|$ .

We see that the cumulative effect of the Heisenberg exchange and the bosonic double exchange results in the stabilization of the  $S = 4$  high-spin (ferromagnetic) state of the EH dimer provided  $|t_B| > 10J$  (see the left panel in Figure 1) and the  $S = 1$  low-spin (“ferrimagnetic”) state otherwise (see right panel in Figure 1). As for the spin states with intermediate  $S$  values ( $S = 2, 3$ ), these correspond to a classical noncollinear ordering. It is interesting that for  $|t_B| = 10J$ , the energy of the dimer’s  $s$ -type state does not depend on the value of the total spin, so that we arrive at the surprising result of the 24-fold ( $\sum_{S=1}^{S=4} (2S+1)$ ) degeneracy of the ground state of an isolated dimer (see the central panel in Figure 1).

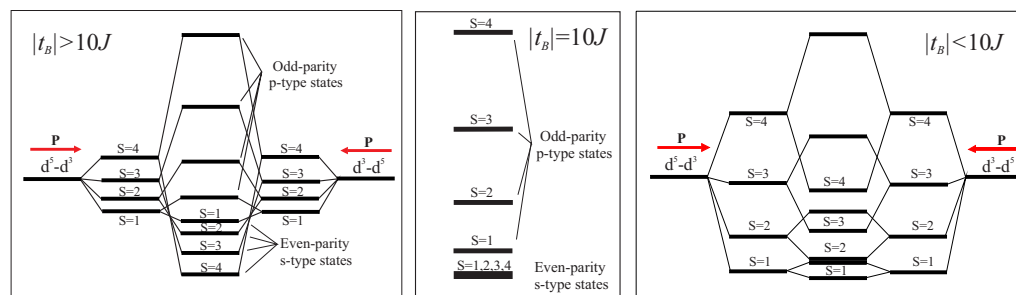


**Figure 1.** (Color online): Spin structure of the EH dimer, or self-trapped CT exciton with a step-by-step inclusion of the one- and two-particle charge transfer. Arrows point to electric dipole moments for bare site-centered dimer configurations.

To estimate quantities  $t_B$  and  $J(d^5d^3)$  and their dependencies on the crystal structure parameters, we can address the results of a comprehensive theoretical and experimental analysis of different superexchange integrals in perovskites  $RFeO_3$ ,  $RCrO_3$ , and  $RFe_{1-x}Cr_xO_3$ , with  $Fe^{3+}$  and  $Cr^{3+}$  ions with electronic configurations of  $d^5$  and  $d^3$ , respectively [52–54]. These perovskites are isostructural with many JT magnets, including  $(Ca,Sr,Ba)FeO_3$ ,  $RMnO_3$ , and  $(Ca,Sr,Ba)RuO_3$ .

Antiferromagnetic kinetic exchange contribution to  $J(e_g e_g)$  related to the  $e_g$  electron transfer to the partially filled  $e_g$ -shell, can be written as follows [53,54]:

$$J(e_g e_g) = \frac{(t_{ss} + t_{\sigma\sigma} \cos \theta)^2}{2U}, \quad (20)$$

while for the  $d^5$ - $d^3$  superexchange, we encounter competition between the antiferromagnetic and ferromagnetic contributions

$$J_{FeCr} = J(d^5 d^3) = \frac{2}{15} \left( \frac{t_{\sigma\pi}^2}{U} \sin^2 \theta + \frac{t_{\pi\pi}^2}{U} (2 - \sin^2 \theta) \right) - \frac{\Delta E(35)}{10U} \left[ \frac{(t_{ss} + t_{\sigma\sigma} \cos \theta)^2}{U} + \frac{t_{\sigma\pi}^2}{U} \sin^2 \theta \right]. \quad (21)$$

Here,  $\theta$  is the cation–anion–cation-bonding angle,  $t_{\sigma\sigma} > t_{\pi\sigma} > t_{\pi\pi} > t_{ss}$  are positive definite  $d$ - $d$  transfer integrals,  $U$  is the mean  $d$ - $d$  transfer energy (effective correlation energy), and  $\Delta E(35)$  is the energy separation between  ${}^3E_g$  and  ${}^5E_g$  terms for the  $t_{2g}^3 e_g$  configuration.

Microscopically derived angular dependencies of the superexchange integrals  $J_{FeFe}$ ,  $J_{CrCr}$ , and  $J_{FeCr}$  nicely describe the full set of experimental data on the value of  $T_N$  for various orthoferrites, orthochromites, mixed ferrites–chromites, as well as Mössbauer data on Fe-substituted orthochromites [52–54].

Figure 2 shows the dependence of the superexchange integrals  $J_{FeCr} = J(d^5 d^3)$  and  $J(e_g e_g) = -t_B$  on the cation–anion–cation superexchange angle, which is typical for orthoferrites and orthochromites. The empty rectangles for  $J(d^5 d^3)$  reproduce the experimental data [52], taking into account the measurement errors of the exchange integrals and the average values of the superexchange bonding angles. The dashed curve in Figure 2 describes the angular dependence (20) for  $J(e_g e_g)$  with quantitative estimates based on the analysis of the full set of experimental data on the value of exchange parameters for orthoferrites and orthochromites [52–54].

The fitting allows us to predict the sign change for  $J_{FeCr}$  at  $\theta_{cr} \approx 160$ – $170^\circ$ . In other words, the  $(t_{2g}^3 e_g^2 - O^{2-} - t_{2g}^3)$  superexchange coupling becomes ferromagnetic at  $\theta \geq \theta_{cr}$ .

At variance with  $J(d^5 d^3)$ , the exchange parameter  $J(e_g e_g) \approx |t_B|$  declines rapidly with the decrease in the bonding angle  $\theta$ , so that at  $\theta_{cr} \approx 142^\circ$ , the ferro- and antiferromagnetic contributions to the effective exchange parameter are compensated,  $J_{eff} = J(d^5 d^3) - 0.1|t_B|$ , with  $S = 1, 2, 3, 4$  degeneracy, and there is a transformation of the spin ground state from  $S = 4 \rightarrow S = 1$ , with a ten-fold reduction in the effective transfer integral of the composite boson (see Equation (16)).

We believe that the results of the analysis of the angular dependence of parameters  $J(d^5 d^3)$  and  $J(e_g e_g)$ , presented in Figure 2, can be used to analyze the spin structures of EH dimers in JT magnets with a perovskite structure, such as manganites, ferrates, and ruthenates (see Table 1).

So, for example, for the superexchange geometry, which is typical for  $LaMnO_3$  [55], with the Mn–O–Mn bonding angle  $\theta \approx 155^\circ$ , we find  $J(d^5 d^3) \approx +7$  K and  $J(e_g e_g) \approx |t_B| \approx 297$  K. In other words, for the effective exchange integral  $J_{eff}$ , we arrive at a rather large value:  $J_{eff} = J(d^5 d^3) - 0.1|t_B| \approx -23$  K. Despite the antiferromagnetic sign of the Heisenberg superexchange integral, these data unambiguously point to a dominant fer-

romagnetic contribution from the bosonic double exchange mechanism, with a ground ferromagnetic  $S = 4$  spin state for the EH dimer and a maximal, “nonreduced” value of the composite boson transfer integral.

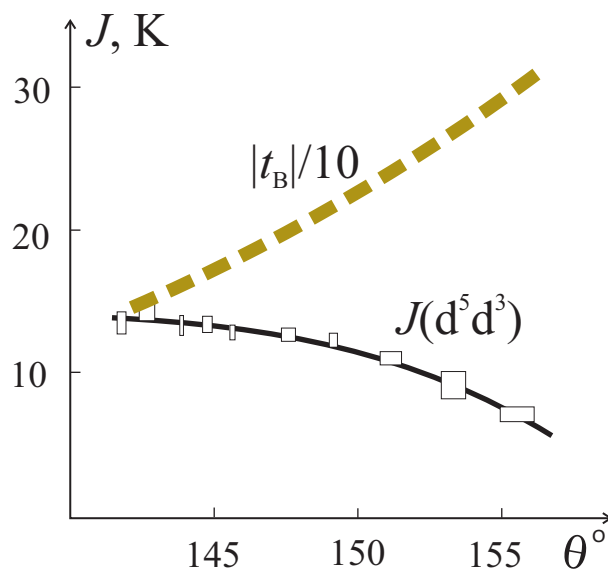


**Figure 2.** (Color online): Angular dependencies of  $J(d^5 d^3)$  and  $\frac{1}{10}|t_B|$ , which define the effective integral  $J_{eff} = J(d^5 d^3) - 0.1|t_B|$ .

For the bonding angle,  $\theta = 143^\circ$ , which is typical for heavy rare-earth manganites  $\text{RMnO}_3$  ( $R = \text{Dy, Ho, Y, Er}$ ) [55], the relationship between  $|t_B| \approx 154 \text{ K}$  and  $J(d^5 d^3) \approx 14 \text{ K}$  [52] approaches to the critical one:  $|t_B| = 10 J(d^5 d^3)$  evidencing the destabilization of the ferromagnetic state of the EH dimers.

Thus, the structural factor plays a significant role in the stabilization of specific spin states of the EH dimer and the effective transfer integral for the composite boson. We believe that the change (decrease) in the angle of the cation–anion–cation superexchange bond, leading to the suppression of ferromagnetic interaction and metallicity, can be the main reason for the strong effect of substituting Sr with Ca in JT magnets, such as  $\text{SrFeO}_3$ ,  $\text{SrRuO}_4$ ,  $\text{Sr}_2\text{RuO}_4$ , and  $\text{Sr}_3\text{Ru}_2\text{O}_7$ .

## 5. Possible Phase States of JT Magnets with Instability to Charge Transfer

In the limit where electron correlations are strong, and potential energy prevails for valence electrons, the stable against charge transfer “progenitor” JT-systems, as a rule, typically manifest as spin-magnetic insulators with a specific orbital ordering (OO), as a consequence of the cooperative JT effect [2]. Conversely, in the limit of weak correlations where the kinetic energy for valence electrons predominates, we arrive at a system of itinerant electrons constituting a Fermi liquid.

In the crossover CT-instability regime, instead of a single inactive charge  $d^n$  component, the on-site Hilbert space of  $d$ -centers includes a charge triplet of  $d^n, d^{n\pm 1}$ -centers, leading to the appearance of at least eight parameters of diagonal and off-diagonal charge orders [43]. Taking into account the spin degree of freedom and lattice modes, we arrive at a huge variety of possible phase states. The phase diagram’s complexity originates from the specific crystal chemistry and a fine balance between the energies of the electron–lattice interaction, crystal field, local (Coulomb and exchange, or Hund) correlations, nonlocal charge correlations, inter-site single and two-particle (composite boson) charge transfers, and spin–spin exchanges. The inevitable consequences of the competitions of many order parameters will be phase separation and the possibility of fine-tuning physical properties by changing the chemical composition, applying external pressure, and going over to epitaxial films and heterostructures.

Taking into account the coexistence of one- and two-particle transports, the high-temperature disordered phase for these systems will be a kind of “boson-fermion soup” [56], or a “strange/bad” metal with a  $T$ -linear resistance dependence (strange metal) and a violation of the Mott–Ioffe–Regel criterion (bad metal). Indeed, the “strange/bad” metal behavior is common in all the JT magnets listed in Table 1.

A specific long-range order in JT magnets starts to form at a high temperature in a disordered phase, which is characterized by the competition between the electron–lattice interaction, and spin and charge fluctuations in the “struggle” for the low-temperature ground state. The local JT interaction leads to the stabilization of low-symmetry-insulating magnetic structures. Low-energy charge fluctuations, which are characteristic of the local anti-JT disproportionation reaction (1), depend on the ratio between the parameters of local and non-local correlations, the integrals of one- and two-particle transfers, and the specifics of the electron–lattice interaction associated with the breathing mode unique to electron–hole pairs; this can lead to the formation of a wide variety of phases, including charge (CO) and spin–charge ordering, collinear and noncollinear magnetic ordering, a coherent metallic Fermi liquid FL phase, a bosonic superconductivity (BS) phase, and a specific nematic phase with the EH dimer ordering [43,57].

It should be noted that materials that are simultaneously magnetic and charge-ordered can be multiferroic, with potentially very large electric polarization.

We believe that the expected superconductivity of JT magnets is not a consequence of the BCS-type pairing, but the result of a quantum transport of the effective on-site composite electron/hole bosons. The superconducting state, as one of the possible ground states of JT magnets, can compete with the normal Fermi liquid state, charge order, spin–charge density wave, collinear or noncollinear magnetic orders, as well as specific quantum phases. The variety of competing phases clearly indicates the important role of phase separation effects [43,58], which must be taken into account first when analyzing experimental data.

Below, without dwelling on a detailed analysis of phase states and phase diagrams, we consider only the main features of the single- and two-band JT magnets in fully disproportionated states, when they form a system of spin–singlet or spin–triplet composite bosons in a nonmagnetic or magnetic lattice, respectively. Strictly speaking, to describe the disproportionate systems, it is necessary to take into account the electron–lattice interaction, primarily with the so-called breathing mode; below, we will consider the effective Hamiltonian of effective composite bosons in the “frozen” lattice approximation.

## 6. Single-Band JT Magnets

### 6.1. Effective Hamiltonian of a System of Spin–Triplet Composite Bosons: Non-Magnetic Lattice

As can be seen in Table 1 the anti-Jahn–Teller disproportionation in the system of tetrahedral JT centers with a configuration of  $3d^1$ ,  $4d^1$ , low-spin octa-centers with configurations of  $3d^7$ ,  $4d^7$ , or octa-centers with configurations of  $3d^9$ ,  $4d^9$  leads to the formation of a half-filled system of effective spin–triplet bosons moving in a non-magnetic lattice. We represent the Hamiltonian of such a system in the following form:

$$\mathcal{H} = - \sum_{i>j,\nu} t_{ij} (\hat{B}_{i\nu}^\dagger \hat{B}_{j\nu} + \hat{B}_{i\nu} \hat{B}_{j\nu}^\dagger) + \sum_{i>j,\nu,\nu'} V_{ij} n_{i\nu} n_{j\nu'} - \sum_{i,\nu} \mu_\nu n_{i\nu} + \mathcal{H}_s, \quad (22)$$

where  $t_{ij}$  is the spin-independent boson transfer integral,  $V_{ij}$  is the effective boson–boson repulsion (nonlocal correlations),  $\mu$  is the chemical potential,  $\mathcal{H}_s$  is the spin Hamiltonian. The chemical potential  $\mu$  is introduced to fix the boson concentration  $n = \frac{1}{N} \sum_{i\nu} \langle \hat{n}_{i\nu} \rangle$ .

The composite boson creation/annihilation operators  $\hat{B}_{i\nu}^\dagger / \hat{B}_{i\nu}$ , regardless of the spin component  $\nu = 0, \pm 1$ , obey the on-site anti-commutation Fermi relations and the inter-site Bose commutation relations:

$$\{\hat{B}_i, \hat{B}_i^\dagger\} = 1, [\hat{B}_i, \hat{B}_j^\dagger] = 0. \quad (23)$$

The anti-commutation Fermi relations can be rewritten as

$$[\hat{B}_i, \hat{B}_i^\dagger] = 1 - 2\hat{B}_i^\dagger \hat{B}_i = 1 - 2\hat{N}_i. \quad (24)$$

On the whole, these relations rule out on-site double-filling.

To take into account the influence of an external magnetic field, one can use the standard Peierls substitution:

$$t_{ij} \rightarrow t_{ij} e^{i(\Phi_j - \Phi_i)}, \quad (25)$$

with

$$(\Phi_j - \Phi_i) = -\frac{q}{\hbar c} \int_{\mathbf{R}_i}^{\mathbf{R}_j} \mathbf{A}(\mathbf{r}) d\mathbf{l}, \quad (26)$$

where  $\mathbf{A}$  is the vector potential of a homogeneous magnetic field, and the integration goes along the line connecting the sites  $i$  and  $j$ . In a general case, the spin Hamiltonian, denoted as  $\mathcal{H}_s$  for the system of spin-triplet bosons, can be represented as follows:

$$\mathcal{H}_s = \sum_{i>j} J_{ij} (\hat{\mathbf{s}}_i \cdot \hat{\mathbf{s}}_j) + \sum_{i>j} j_{ij} (\hat{\mathbf{s}}_i \cdot \hat{\mathbf{s}}_j)^2 + K_{SIA} \sum_i (\mathbf{m}_i \cdot \hat{\mathbf{s}}_i)(\mathbf{n}_i \cdot \hat{\mathbf{s}}_i) + V_{TIA} - \sum_i (\mathbf{h} \cdot \hat{\mathbf{s}}_i), \quad (27)$$

where  $J_{ij}$  and  $j_{ij}$  are the bilinear and biquadratic isotropic exchange integrals, respectively,  $K_{SIA}$  is a constant,  $\mathbf{m}$  and  $\mathbf{n}$  are unit vectors that define two characteristic axes of the second-order single-ion anisotropy,  $V_{TIA}$  denotes the two-ion bilinear and biquadratic anisotropy, and  $\mathbf{h}$  denotes the external field.

It is worth noting that the Cartesian form of the composite boson spin operator can be represented as follows

$$\hat{s}_\beta = \hat{B}_\alpha^\dagger \epsilon_{\alpha\beta\gamma} \hat{B}_\gamma, \quad (28)$$

where  $\epsilon_{\alpha\beta\gamma}$  is Levi-Civita tensor,  $\alpha, \beta, \gamma = x, y, z$ .

In the paramagnetic region, the Hamiltonian (27) actually reduces to the Hamiltonian of the well-known lattice hard-core (*hc*) Bose system with an inter-site repulsion, governed in the nearest-neighbor approximation by two parameters,  $t_B$  and  $V$ . At half-filling, depending on the relative values of the parameters, we arrive at a charge order (CO) or Bose-superfluid (BS) phase. As the temperature decreases, a specific magnetic order is realized in the system.

## 6.2. $d^1, d^3$ JT Magnets

The only JT magnets that are known in the literature with tetrahedral  $d^1$ -centers, such as  $\beta$ - $\text{Sr}_2\text{VO}_4$  with  $\text{V}^{4+}$  and  $(\text{Sr}, \text{Ba})_3\text{Cr}_2\text{O}_8$  with  $\text{Cr}^{5+}$ , are considered to be typical insulators, exhibiting Jahn–Teller distortions with orbital ordering and the formation of a system of weakly coupled spin dimers (see, e.g., Refs. [59–61]). We did not find any literature data on JT magnets with tetrahedral  $d^3$ -centers, except for the assumption made in Ref. [62] about the possibility of synthesizing  $\text{Ba}_2\text{VGe}_2\text{O}_7$  melilite with  $\text{V}^{2+}$  ions, an anticipated JT-multiferroic.

## $d^7$ JT Magnets

The origin of the metal-to-insulator transition (MIT) in the series of rare-earth nickelates  $\text{RNiO}_3$  with perovskite structures has challenged the condensed matter research community for almost three decades [63]. Furthermore, the recent theoretical prediction for superconductivity in  $\text{LaNiO}_3$  thin films [64] has also sparked intensive research efforts.

The complex MIT phenomena in these materials are a perfect illustration of the competition between the potential and kinetic energy gain, presumably governed by structural factors, namely, the Ni–O–Ni bond angle, providing clear evidence for strong electron–lattice effects, which have a dramatic effect on the character of the MIT.

Orthorhombic  $\text{RNiO}_3$  ( $R = \text{Pr}, \dots \text{Lu}$ ) undergoes a first-order metal–insulator phase transition to a charge-ordered insulating state upon cooling below  $T_{\text{CO}} = T_{\text{MIT}}$ , spanning from 130 K for Pr to  $\sim 550$ – $600$  K for heavy rare-earth [63]. Each shows clear signs of the charge-disproportionated state with two types of Ni centers that correspond to alternating large  $[\text{NiO}_6]^{10-}$  ( $\text{Ni}^{2+}$  center) and small  $[\text{NiO}_6]^{8-}$  ( $\text{Ni}^{4+}$  center) octahedra, strongly differing in magnetic moments ( $\sim 2 \mu_B$  and  $\sim 0$ , respectively), in full accordance with the disproportionation model (see Table 1). The largest anomaly at  $T_{\text{MIT}} = T_N = 130$  K in  $\text{PrNiO}_3$  is observed in the amplitude of the breathing mode, which undergoes a sharp jump of  $0.15 \text{ \AA}$  [65]. A further interesting observation is the existence of a nearly perfect linear correlation between the amplitude of the breathing mode associated with the charge order and the staggered magnetization below the MIT. In addition, the authors [65] suggest the existence of hidden symmetry in the insulating phase, which may be related to a nematic contribution of bound EH dimers.

At low temperatures, ortho-nickelates show magnetic phase transitions toward unusual antiferromagnetic structures defined by a propagation vector  $(1/2, 0, 1/2)$  [63], which can be explained by the rather strong superexchange  $nmn$  (next-nearest neighbor) coupling of magnetic  $S = 1 \text{ Ni}^{2+}$  centers. Strictly speaking, the  $(1/2, 0, 1/2)$  ordering suggests three possible magnetic structures, of which, two are collinear and one is non-collinear. For instance, a spin-canted antiferromagnetic state of the nickel sublattice was observed in  $\text{NdNiO}_3$  [66]; however, the ambiguity of the magnetic structure of the nickelates is not yet completely resolved. The non-collinear spin order in nickelates can potentially generate spin-induced ferroelectricity; however, these systems remain comparatively unexplored as potential multiferroics [67].

Increasing the Ni–O–Ni bond angle in nickelates when moving from  $\text{LuNiO}_3$  to  $\text{LaNiO}_3$  leads to a gain in kinetic energy with a clear trend toward metallization due to two important effects, namely, an increase in the transfer integrals for the  $e_g$  electrons and a decrease in parameter  $V$  of inter-site repulsion (nonlocal correlations), due to an increase in the Ni–Ni separation. So, the X-ray diffraction, neutron scattering, transport, and thermodynamic experiments show that globally rhombohedral single-crystal  $\text{LaNiO}_3$  samples reveal unusually high metallicity and maintain paramagnetic behavior down to 1.8 K [68], or some signatures of antiferromagnetic transition at 157 K [69], but no structural and metal–insulator transitions. The combined total neutron scattering and broadband dielectric spectroscopy experiments on polycrystalline samples [70] indicate that the structure of  $\text{LaNiO}_3$  has a high degree of symmetry when viewed on long-length scales, but similar to orthorhombic nickelates, it also has at least two different types of Ni sites when viewed locally.  $\text{LaNiO}_3$  is locally distorted to orthorhombic at room temperature, and further to monoclinic at 200 K from a globally rhombohedral structure [71]. This controversial behavior for  $\text{LaNiO}_3$  can be the result of the peculiar “ortho-mono-rhombo” phase separation.

Another example of nickel JT magnets is the quasi-2D nickelates  $\text{ANiO}_2$  ( $A = \text{Ag}, \text{Li}, \text{Na}$ ), revealing the existence of unconventional ground states stabilized by the frustrated triangular lattice geometry from a cooperative JT ordering of  $\text{Ni}^{3+}$  ions in  $\text{NaNiO}_2$  to a moderately charged ordering  $3\text{Ni}^{\text{III}+} \rightarrow \text{Ni}^{2+} + 2\text{Ni}^{3.5+}$  in antiferromagnetic metal  $\text{AgNiO}_2$  [72]. In the case of  $\text{LiNiO}_2$ , there could be a competition between charge and orbital ordering, the nickel valency could be a mixture of 2+, 3+, and 4+ [73]. A comparison between  $\text{NaNiO}_2$  and  $\text{LiNiO}_2$ , where several different possible ground states are very close in energy, illustrates how two systems that are apparently so chemically similar can, nevertheless, have very different behavior [73].

### 6.3. $d^9$ JT Magnets

#### 6.3.1. Isoelectronic Quasi-2D Cuprates and Nickelates

The  $\text{Cu}^{2+}$  ion in octahedral complexes is characterized by the strongest JT bond and is the most popular, almost “textbook” illustration of the Jahn–Teller effect. The consequence of this effect is the formation of the insulating state of a quantum antiferromagnet, for example, in  $\text{KCuF}_3$  and  $\text{La}_2\text{CuO}_4$ , or quasi-2D ferromagnet  $\text{K}_2\text{CuF}_4$ . However, in contrast

to fluorides, in  $\text{La}_2\text{CuO}_4$ , the JT distortion leads to the formation of  $\text{CuO}_2$  planes with a “perovskite” configuration of  $\text{CuO}_4$ -clusters, with the ground  $b_{1g} \propto d_{x^2-y^2}$  state of the  $e_g$  hole, which provides a strong  $\sigma$ -coupling channel for the hole transfer in the  $\text{CuO}_2$  plane and disproportionation (2), forming spin-singlet and orbitally nondegenerate ( $^1A_{1g}$ ) electronic  $[\text{CuO}_4]^{7-}$  (analog of  $\text{Cu}^+$  ion) and Zhang–Rice (ZR) [74] hole  $[\text{CuO}_4]^{5-}$  (analog of the  $\text{Cu}^{3+}$  ion) centers.

Recently [43,45], we argued that there are no fundamental qualitative differences in the electronic structures of “apex-free”  $\text{RNiO}_2$  nickelates and cuprates (primarily, cuprates with  $T'$ -structures). The unusual properties of cuprates and nickelates are the results of the “competition” between various parameters that govern the ground states of the  $\text{CuO}_2$  ( $\text{NiO}_2$ ) planes. Thus, if for the vast majority of parent cuprates, an antiferromagnetic insulating phase is observed, corresponding to the limits of strong local correlations, then this phase is not found in the parent nickelates  $\text{RNiO}_2$ , which can be associated with smaller values or even a change in the sign of the local correlation parameter. We proposed [43,45] to understand by “parent” the cuprates and nickelates with hole half-fillings of in-plane centers  $\text{CuO}_4$  ( $\text{NiO}_4$ ), which—depending on the parameters of local and non-local correlations, transfer integrals, exchange integrals, and “external” crystal fields formed by the out-of-plane environment—can have different ground states, e.g., an antiferromagnetic insulator (AFMI), an unusual Bose superconductor (BS), a Fermi metal (FL), or a non-magnetic insulator with charge ordering (CO). Obviously, these phases will differ in electronic degrees of freedom as well as lattice degrees of freedom; this interaction ensures the minimum of the total free energy. In addition, the competition between several possible phases with similar energies will lead to phase separation, which will have a significant effect on the observed physical properties.

To describe the actual low-energy phase states of cuprates/nickelates, we propose a minimal model for the  $\text{CuO}_2/\text{NiO}_2$  planes with the on-site Hilbert space reduced to a charge triplet of the three effective valence centers  $[\text{CuO}_4]^{5-,6-,7-}/[\text{NiO}_4]^{6-,7-,8-}$  (nominally,  $\text{Cu}^{3+,2+,1+}/\text{Ni}^{2+,1+,0+}$ ) with different conventional spins, different orbital symmetries, and local lattice configurations [43–45,58,75–78]. Making use of the  $S = 1$  pseudospin formalism and the spin-pseudospin operators as the Hubbard  $X$ -operators, we constructed the spin-pseudospin Hamiltonian of the charge triplet model, which takes into account local and nonlocal correlations, correlated one-particle and two-particle (bosonic) transports, and the Heisenberg spin exchange. In particular cases, the Hamiltonian reduces to a well-known “limiting” Hamiltonian (Hubbard, Heisenberg, atomic limit, hard-core bosons, ...). In accordance with experimental data for apexless cuprates [79], nickelates [80], and different typical cuprates, we argue that antiferromagnetic insulating (AFMI), charge ordered (CO), Bose superconducting (BS), and Fermi liquid (FL) phases are possible phase states of a model parent cuprate/nickelate, while typical phase states of doped systems, in particular, mysterious pseudogap phases, are the result of a phase separation (PS). The superconductivity of cuprates/nickelates is not a consequence of the pairing of doped holes [30], but the result of the quantum transport of on-site composite hole bosons, whereas the main peculiarities of a normal state can be related to an electron-hole interplay for an unusual Fermi liquid phase and PS features. In the BCS model, the electron-lattice interaction determines the  $s$ -wave pairing, while in the model of local composite bosons, it yields the  $d_{x^2-y^2}$ -symmetry of the superconducting order parameter, thus showing, once again, a substantial involvement of the lattice in the HTSC [43,44]. Within the framework of the effective field approximation [81] and the Maxwell construction [43–45,58], we constructed several 2D  $T$ - $p$  phase diagrams for the  $\text{CuO}_2/\text{NiO}_2$  planes, which qualitatively reproduce the main features of the experimentally observed 3D phase diagrams of cuprates and nickelates [43] (see Figure 3). Note that the exotic pseudogap phase is believed to be related to the PS region AFMI-CO-FL-BS, separated from the 100% FL-phase by the  $T^*(p)$  curve (“pseudogap temperature”) of the “third order” phase transition.

In general, quasi-2D cuprates and nickelates present excellent examples of the applicability of the anti-JT disproportionation model. A large amount of experimental data from

a long-term study of various properties of a wide class of old 2D cuprates and novel 2D nickelates, as well as the results of the theoretical modeling of phase diagrams in the charge triplet model [43], provide important information about possible phase states of other JT magnets with charge transfer.

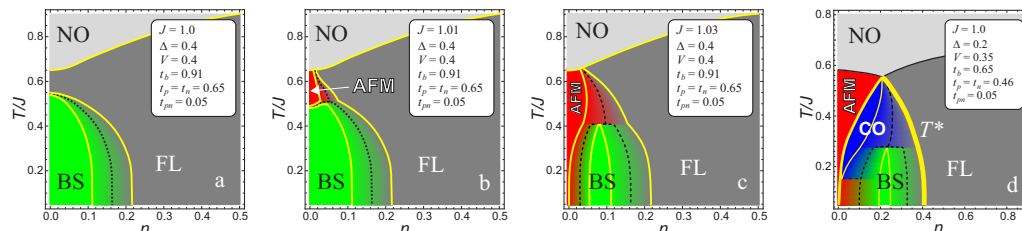


**Figure 3.** (Color online): Model phase  $T$ - $n$ -diagrams of hole-doped  $\text{CuO}_2/\text{NiO}_2$  planes in cuprates/nickelates calculated in the effective field approximation ( $n = p$  for hole doping), with the phase separation taken into account using Maxwell's construction;  $J$  is the exchange integral,  $\Delta = U/2$  is the local correlation parameter,  $V$  is the nonlocal correlation parameter,  $t_p, t_n, t_{pn}$  are three independent integrals of the correlated single-particle transfer,  $t_B$  is the effective transfer integral of the composite boson (see insets), assuming competition between “monophases” NO (disordered), AFMI, BS, FL, and CO. The boundaries between the phases represent lines of equal free energies. The dashed curves (a–d) indicate the lines of equal volume fractions of two neighboring phases, the yellow curves represent the lines of phase transitions of the “third” kind, limiting the regions with maximal 100% volume fractions of one of the phases. See Refs. [43,44] for more details. Pay attention to the strong change in the phase diagram, even with a very small change in the parameters of the Hamiltonian (compare panels a–c).

### 6.3.2. “Silver” JT Magnets

The anti-JT disproportionation model predicts the possibility of a “silver or palladium path” to superconductivity in systems based on  $\text{Ag}^{2+}(4d^9)$  or  $\text{Pd}^+(4d^9)$ ; that is, the 4d analog of  $\text{Cu}^{2+}$ . The most likely candidate, silver fluoride  $\text{AgF}_2$  [82–84], also known as  $\alpha$ - $\text{AgF}_2$ , is an excellent analog of the cuprate with surprisingly close electronic parameters to  $\text{La}_2\text{CuO}_4$ , but with greater deformation (buckling) of  $\text{AgF}_2$  planes. However, this fluoride is a canted antiferromagnetic insulator, although close to a charge-transfer instability. Indeed, experimental studies [85] report the discovery of a metastable disproportionate diamagnetic phase  $\beta$ - $\text{AgF}_2$ , interpreted as a charge-ordered compound  $\text{Ag}^{1+}\text{Ag}^{3+}\text{F}_4$ , which quickly transforms into the  $\alpha$ - $\text{AgF}_2$  structure (see Ref. [86]).

Unlike the antiferromagnetic insulator  $\text{Cu}^{2+}\text{O}$ , its silver 4d analog  $\text{Ag}^{2+}\text{O}$  is a diamagnetic semiconductor with a disproportionate Ag sublattice, whose chemical formula is often written as  $\text{Ag}^{1+}\text{Ag}^{3+}\text{O}_2$ , with  $\text{O}-\text{Ag}^{1+}(4d^{10})-\text{O}$  collinear bonds and  $\text{Ag}^{3+}$  square planar bonds  $(4d^8)\text{O}_4$  [87,88]. In this case, the  $[\text{AgO}_4]^{5-}$  cluster, like the  $[\text{CuO}_4]^{5-}$  center in cuprates, is in a nonmagnetic state of the Zhang–Rice singlet type.

## 7. Two-Band JT Magnets

Single-band JT magnets, with their relatively simple electronic structures, provide an excellent illustration of the predictive power of the anti-JT disproportionation model, while the situation with two-band JT magnets is less certain.

Anti-Jahn–Teller disproportionation in “two-band” systems of high-spin octa centers with  $3d^4, 4d^4$  configurations, or tetrahedral JT centers with  $3d^6, 4d^6$  configurations, imply unusual phases with the coexistence of a half-filled system of effective spin–triplet electrons or hole bosons with configurations of  $e_g^2 : {}^3A_{2g}$  or  $e_g^2 : {}^3A_{2g}$ , and a magnetic lattice with on-site  $S = 3/2$  configurations of  $t_{2g}^3 : {}^4A_{2g}$ , although this does not exclude the existence of unusual phases with delocalized  $t_{2g}$  electrons (see the review article [89]).

Two-band JT magnets include many promising compounds, most of which are presented in the last column of Table 1. Below, we briefly consider the effective Hamiltonian,

the features of the electronic structure, and physical properties of the most prominent representatives of two-band JT magnets.

### 7.1. Effective Hamiltonian of a System of Spin-Triplet Composite Bosons: Magnetic Lattice

The anti-Jahn–Teller disproportionation in a system of high-spin octahedral JT-centers with  $3d^4$ ,  $4d^4$  configurations or tetrahedral JT-centers with  $3d^6$ ,  $4d^6$  configurations leads to the formation of a half-filled system of effective spin-triplet electron or hole bosons with configurations of  $e_g^2 : {}^3A_{2g}$  or  $e_g^2 : {}^3A_{2g}$ , moving in a magnetic lattice with on-site configurations of  $t_{2g}^3 : {}^4A_{2g}$  (see Table 1).

The effective Hamiltonian of such a system can also be represented as (22), however, with the spin-dependent composite boson transfer integral (see Equation (16))

$$t_{ij} = \frac{S(S+1)}{20} t_B, \quad (29)$$

where  $\hat{S} = \hat{S}_i + \hat{S}_j$  is the total spin of the EH-pair ( $ij$ ),  $S = 1, 2, 3, 4$ .

In contrast with the single-band JT magnets, the spin Hamiltonian  $\mathcal{H}_s$  for two-band JT magnets will have a much more complex structure. Taking into account only the bilinear spin–spin isotropic exchange, it can be represented as follows:

$$\mathcal{H}_s = \sum_{i>j} J_{ij}^{ll} (\hat{S}_i \cdot \hat{S}_j) + \sum_{i>j} J_{ij}^{bb} (\hat{s}_i \cdot \hat{s}_j) + \sum_{i>j} J_{ij}^{bl} (\hat{s}_i \cdot \hat{S}_j) + \sum_i J_{ii}^{bl} (\hat{s}_i \cdot \hat{S}_i), \quad (30)$$

where we assume the localized  $t_{2g}$  subshell. The first term denotes the exchange interaction between the “lattice” spins, the second term denotes the exchange interaction between the spin-triplet bosons, the third and fourth terms denote the exchange between bosons and lattice spins, and the last term denotes the intra-atomic Hund exchange. To fulfill Hund’s rule, it is necessary to set the exchange integral  $J_{ii}^{bl}$  to be relatively large ferromagnetic.

Estimates for different superexchange couplings—given the cation–anion–cation bond geometry that is typical for perovskites such as ferrates (Ca,Sr)FeO<sub>3</sub> or manganites RMnO<sub>3</sub> with bare octa-HS  $d^4$  configurations [51]—predict the antiferromagnetic coupling for the  $nn$  lattice centers ( $J^{ll} > 0$ ) and the two nearest neighbor bosons ( $J^{bb} > 0$ ), where the coupling between the boson and the nearest neighbor lattice centers ( $J^{bl} < 0$ ) can be ferro- or antiferromagnetic, depending on the value of the cation–anion–cation-bonding angle (see Figure 1). Taking into account the boson transport, which prefers an overall ferromagnetic ordering, we arrive at a highly frustrating system with competition between the ferro- and antiferromagnetic interactions.

Generally speaking, our Hamiltonian model describes the system that can be considered a Bose analog of the *one-orbital* double-exchange model system [90].

### 7.2. Chromium Cr<sup>2+</sup> Compounds

Among the JT chromium compounds, we—more or less—have reliable information about chromium difluoride CrF<sub>2</sub>, according to which, it is an antiferromagnetic insulator [91]. However, X-ray absorption and resonant inelastic X-ray scattering (RIXS) spectra of CrF<sub>2</sub> [92] point to the presence of three chromium oxidation states, namely Cr<sup>+</sup>, Cr<sup>2+</sup>, and Cr<sup>3+</sup>, indicating instability with respect to the charge transfer, with clear signatures of the  $d$ - $d$  disproportionation reaction in this JT magnet. The most likely explanation for this is phase separation; that is, the coexistence of antiferromagnetic regions and regions of a disproportionate phase.

### 7.3. Manganites RMnO<sub>3</sub>

Features of the anti-JT disproportionation and its influence on the phase diagram of manganites RMnO<sub>3</sub> are considered in detail in Ref. [51].

A high-temperature, thermally fluctuating charge disproportionated metallic state has been postulated for LaMnO<sub>3</sub> by different authors [93–95]. However, upon lowering the

temperature, one observes a first-order phase transition at  $T = T_{JT}$  ( $T_{JT} \approx 750$  K in  $\text{LaMnO}_3$ ) from the high-temperature fully disproportionate Bose metallic phase to a low-temperature orbitally ordered insulating phase, with a cooperative Jahn–Teller ordering of the occupied  $e_g$ -orbitals of the  $\text{Mn}^{3+}\text{O}_6$  octahedra, accompanied by A-type antiferromagnetic ordering below  $T_N$  ( $T_N \approx 140$  K in  $\text{LaMnO}_3$ ) [51,95]. However, many experimental data point to a phase separation with the coexistence of insulating and disproportionated phases [51,96].

The non-isovalent substitution and/or non-stoichiometry seem to revive the disproportionated phase, and such manganites—along with metallic ferromagnetism and colossal magnetoresistance—reveal many properties that are typical for local spin–triplet superconductivity [51,97–102].

Distinct signatures of high-temperature disproportionated phases are revealed in other manganites, such as  $\text{LaMn}_7\text{O}_{12}$  [103] with quadruple perovskite structures and  $\text{YBaMn}_2\text{O}_6$  [104].

Additionally, the orthorhombic rare-earth manganites  $\text{RMnO}_3$  characteristically display non-collinear spin–spiral orders and form a “model family” of spin-driven ferroelectrics [67].

#### 7.4. Iron $\text{Fe}^{4+}$ JT Magnets

All the ferrates listed in Table 1, are JT magnets that are unstable with respect to charge transfer.

The  $\text{AFe}^{4+}\text{O}_3$  ( $\text{A} = \text{Ca}, \text{Sr}, \text{Ba}$ ) perovskites show intriguing physical properties, which are strongly dependent on the size and polarizability of the A-site ion since this affects all the main parameters governing their electronic structures.

With decreasing temperatures, orthorhombic metallic  $\text{CaFeO}_3$  (CFO) exhibits a second-order phase transition to a narrow-gap charge-ordered monoclinic semiconductor, or Hund’s insulator, with disproportionation in  $\text{Fe}^{4\pm\delta}$  below a transition temperature  $T_{CO} = T_{MIT} = 290$  K at ambient pressure, resulting in a three-dimensional rock salt-type ordering of alternating small and large oxygen octahedra surrounding the nominal  $d^3$  and  $d^5$  Fe sites, respectively [38]. Parameter  $\delta = 0$  for  $T > 290$  K increases continuously with decreasing temperatures below 290 K; typically,  $\delta$  approaches unity at low temperatures. The MIT is accompanied by the reduction in crystal symmetry as well as the sharp variation in electrical transport. Within our model, the disproportionated phase in the CFO implies the electron boson confinement in the larger  $\text{FeO}_6$  octahedra.

The charge disproportionation scenario for CFO has been experimentally well-established using  $^{57}\text{Fe}$  Mössbauer spectroscopy [105,106], which clearly reveals two different sites with considerably different isomer shifts and hyperfine fields.

Let us pay attention to the possibility of the formation of domains in the charge-ordered state with  $180^\circ$ -domain walls, realizing the transition between two types of “site-centered” charge orders. At the center of the domain walls, a system of delocalized spin–triplet composite bosons with a “bond-centered” charge order is formed, which formally corresponds to the system of  $\text{Fe}^{4+}$  centers.

As the temperature is further lowered, there is another transition in the CFO from the paramagnetic to an antiferromagnetic insulator at the Néel temperature  $T_N \approx 120$  K. The low-temperature magnetic data can be fit equally well by a screw–spiral structure or by a sinusoidal amplitude-modulated structure. The values of the moments at the two Fe sites can take different values; 2.5 and 3.5  $\mu_B$  for the spiral structure, and maximum amplitudes of 3.5 and 5.0  $\mu_B$  for the sinusoidal structure [38].

Note that the high-temperature orthorhombic metal phase of CFO can be considered as a Hund’s bad metal, which appears as a mixed-valence state that fluctuates between two atomic configurations.

In contrast to the distorted perovskite  $\text{CaFeO}_3$ , the undistorted cubic perovskites  $\text{SrFeO}_3$  and  $\text{BaFeO}_3$  maintain metallic behaviors down to very low temperatures, exhibiting different types of helical spin order. However, the ground states in these ferrates raise many questions. At variance with Mössbauer data for  $\text{CaFeO}_3$ , the single magnetic hy-

perfine pattern for SrFeO<sub>3</sub> at 4 K indicates a rapid electron exchange between Fe<sup>3+</sup> and Fe<sup>5+</sup> ions; the center shift and the hyperfine field coincide approximately with the average values of the corresponding parameters for CaFeO<sub>3</sub> [105]. In other words, “static” disproportionation occurs in CaFeO<sub>3</sub> with the formation of a site-centered charge order, whereas in SrFeO<sub>3</sub>, we are dealing with “dynamic” disproportionation, with the formation of a bond-centered charge order. Furthermore, in SrFeO<sub>3</sub>, experiments have revealed a phase-separated state with a surprising variety of magnetic incommensurate helical and commensurate structures [107].

Surprisingly, a ferromagnetic ground state is found in BaFeO<sub>3</sub> single-crystalline thin films with a saturation magnetization and Curie temperature of 3.2 μ<sub>B</sub>/formula unit and 115 K, respectively [108]. Unusually, for a uniform cubic ferromagnet, the films are insulating, possessing an optical gap of ~1.8 eV.

The incommensurate helicoidal spin ordering observed in both CaFeO<sub>3</sub> and SrFeO<sub>3</sub> [109], up to very low temperatures, can be explained as a result of the competition between conventional exchange coupling and the bosonic double exchange. Obviously, the theoretical and experimental studies of the phase diagram for (Ca,Sr)FeO<sub>3</sub> and substituted systems deserve further exploration, especially, investigations aimed at exploring possible superconductivity.

The <sup>57</sup>Fe Mössbauer measurements for the double-layered perovskite ferrate Sr<sub>3</sub>Fe<sub>2</sub>O<sub>7</sub> indicate the charge disproportionation and the magnetic properties, which are similar to CaFeO<sub>3</sub> [110]. The critical temperature for the charge disproportionation reaction and the Néel temperature T<sub>N</sub> of the helical spin order are determined to be ~343 K and ~120 K, respectively. Above 343 K, spectra clearly show a Fe<sup>4+</sup> singlet. Puzzlingly, the spatial ordering pattern of the disproportionated charges has remained “hidden” to conventional diffraction probes, despite numerous X-ray scattering and neutron scattering studies. Only relatively recently, by making use of neutron Larmor diffraction and Fe K-edge resonant X-ray scattering, Kim et al. [111] demonstrated the checkerboard charge order in the FeO<sub>2</sub> layers and showed that the “invisibility” of charge ordering in Sr<sub>3</sub>Fe<sub>2</sub>O<sub>7</sub> originates from the frustration of the interactions between neighboring layers.

The less-studied quasi-2D ferrate Sr<sub>2</sub>FeO<sub>4</sub> with the K<sub>2</sub>NiF<sub>4</sub> structure is a compound isotypic with the parent cuprate La<sub>2</sub>CuO<sub>4</sub>. It is an antiferromagnetic semiconductor at ambient pressure with a Néel temperature T<sub>N</sub> of about 56 K [112,113]. In the past 30 years, the concept of the electronic structure of Sr<sub>2</sub>FeO<sub>4</sub> has changed from a Mott-type antiferromagnetic insulator similar to La<sub>2</sub>CuO<sub>4</sub> [112] to an insulator with negative charge-transfer energy (negative-Δ<sub>pd</sub>) [113]. The insulating ground state of Sr<sub>2</sub>FeO<sub>4</sub> is assumed to be stabilized by a hidden structural distortion similar to the charge order in the related Sr<sub>3</sub>Fe<sub>2</sub>O<sub>7</sub>, and differs from the charge disproportionation in other Fe<sup>4+</sup> oxoferrates.

However, we believe that the ground spin–charge state in this ferrate, as well as in other JT ferrates, is determined by *d*–*d* anti-JT disproportionation. This is evidenced by the absence of a noticeable JT distortion of the FeO<sub>6</sub> octahedra, the manifestation of a phonon mode atypical for the K<sub>2</sub>NiF<sub>4</sub> structure, which can be naturally associated with a breathing mode typical for *d*–*d* disproportionation, an elliptical cycloidal spin spiral structure typical of all JT ferrates, and an insulator–metal transition under high pressure [113]. To elucidate the details of the ground state, we require further studies, particularly on single crystals of Sr<sub>2</sub>FeO<sub>4</sub>.

### 7.5. JT Ruthenates

Just like Fe<sup>4+</sup>(3*d*<sup>4</sup>) JT ferrates, Ru<sup>4+</sup>(4*d*<sup>4</sup>)-based ruthenates belong to the same family of Ruddlesden–Popper (A<sub>*n*+1</sub>B<sub>*n*</sub>O<sub>3*n*+1</sub>) compounds. They host rich physics, including unconventional superconductivity in Sr<sub>2</sub>RuO<sub>4</sub>, a metamagnetic ground state in Sr<sub>3</sub>Ru<sub>2</sub>O<sub>7</sub>, insulating antiferromagnetism in Ca<sub>2</sub>RuO<sub>4</sub> and Ca<sub>3</sub>Ru<sub>2</sub>O<sub>7</sub>, and both paramagnetic and ferromagnetic metallic states in CaRuO<sub>3</sub> and SrRuO<sub>3</sub>, respectively. Ruthenates undergo a variety of electronic, magnetic, and orbital ordering transitions, which are tunable with chemical doping, pressure, temperature, magnetic fields, and epitaxial strain. However,

their properties differ in many points from their 3d analogs. This is due to the fact that the 4d shell of the Ru<sup>4+</sup> ion is more extended than the 3d shell of the Fe<sup>4+</sup> electronic analog, which most likely leads to an increase in the crystal field parameter  $10Dq$ , a decrease in the local correlation parameter, and an increase in the transfer integrals. As a result, the Ru<sup>4+</sup> (4d<sup>4+</sup>) ions tend to adopt a low-spin state or  $S = 1$  state because relatively large crystal fields often overpower the Hund's rule coupling [114].

In other words, in ruthenates, we seemingly encounter a fine high-spin–low-spin (HS–LS) balance, up to the possibility of the coexistence of HS- and LS-states [114,115]. It means that by varying substitutions, tuning the physical and chemical pressures, and reducing the film thicknesses, one can observe different quantum states, ranging from those typical for JT magnets, such as JT ferrates, to states typical for low-spin  $t_{2g}^4$ -systems, with a trend toward phase separation.

Practically all layered ruthenates at low temperatures are characterized by robust Fermi liquid behavior, as evidenced by the quadratic temperature dependence of resistivity and by the observations of quantum oscillations. However, the breach of the Mott–Ioffe–Regel limit for the basal plane resistivity and the anomalous strange metallic behavior, with a linear temperature dependence of resistivity at high temperatures, clearly exhibit behavior inconsistent with any conventional Fermi liquid paradigms [116] but are typical for disproportionate systems with two types of charge transport.

Ruthenates are excellent candidates to explore the intricate interplay between structural and electron–spin degrees of freedom. For instance, Ca<sub>2</sub>RuO<sub>4</sub> is a paramagnetic Mott insulator below the metal–insulator transition temperature  $T_{MIT} \approx 360$  K with antiferromagnetic ordering below  $T_N \approx 110$  K [117]. However, the application of very modest pressure transforms it from the antiferromagnetic Mott insulator to a quasi-2D ferromagnetic metal. Under the current flow, the insulating ground state was observed to transform into an electrically conducting phase with highly diamagnetic susceptibility.

Puzzlingly, single-crystalline Ca<sub>2</sub>RuO<sub>4</sub> nanofilms exhibit the co-appearance of high-temperature superconductivity with  $T_c \approx 60$  K and ferromagnetism [118]. Such a high temperature of the superconducting transition suggests the presence of an unconventional mechanism of superconductivity of the type found in high- $T_c$  cuprates.

The replacement of Ca<sup>2+</sup> ions (ionic radius 1.34 Å) with Sr<sup>2+</sup> ions (ionic radius 1.44 Å) in the bulk family appears to induce a subtle alteration in the electronic structure, while simultaneously leading to a dramatic transformation of the ground state from an antiferromagnetic insulator in Ca<sub>2</sub>RuO<sub>4</sub> to a superconducting and ferromagnetic state in Sr<sub>2</sub>RuO<sub>4</sub>, with a spiral spin structure in the ground normal metallic state [119].

Based on early Knight shift, polarized neutron scattering, muon–spin-resonance, and polar Kerr measurements, Sr<sub>2</sub>RuO<sub>4</sub> has been widely believed to support a spin–triplet chiral  $p$ -wave superconducting state [120]. However, despite significant achievements in characterizing the properties of Sr<sub>2</sub>RuO<sub>4</sub> over the last three decades, the precise nature of its electronic ground state and superconducting order parameter is still unresolved [121,122]. Understanding the nature of superconductivity in Sr<sub>2</sub>RuO<sub>4</sub> is one of the most enigmatic problems in unconventional superconductivity, despite the vast interest and wide array of experiments performed on the material. Recent results have pushed the community toward potentially adopting an even-parity spin–singlet pairing state, although conventional states of this nature are not able to consistently explain all observations. It should be noted that superconductivity is a relatively common property of ruthenates. Very recently, strain-stabilized superconductivity with  $T_c \approx 2$  K was discovered in ruthenate RuO<sub>2</sub> films [123,124].

Generally speaking, despite extensive efforts, a comprehensive understanding of electronic structures and physical properties in JT ruthenates is still lacking.

### 7.6. Iron-Based Superconductors

The Fe<sup>2+</sup> iron-based superconductors have layered structures with the conducting layers made of tetrahedral centers FeAs<sub>4</sub>, FeP<sub>4</sub> (ferropnictides), FeSe<sub>4</sub>, FeS<sub>4</sub>, FeTe<sub>4</sub> (ferrochalcogenides). These JT magnets exhibit the unprecedented richness of physics, some-

times within a single family, encompassing magnetism, unconventional superconductivity, quantum criticality, linear-in-T resistivity, nematic order, and a propensity toward orbital-selective Mott behavior [125–128]. Researchers have found practically all phenomena associated with strongly correlated electron systems in Fe-based materials. At present, a variety of theoretical approaches are being employed to understand these systems, although the issue remains to be fully settled.

Here, our intention is not to deliver a comprehensive review of the electronic structures and phase diagrams of iron-based superconductors, but rather to pay attention to several specific features that allow us to assume an important role of the disproportionation mechanism. Superconductivity in FePn/Ch emerges out of a “bad-metal” normal state and the superconducting phase occurs near the antiferromagnetic order in proximity to a Mott transition. The parent iron pnictides are antiferromagnetically ordered metals; insulating behavior and AF order also appear in a variety of iron chalcogenides.

Unconventional non-BCS superconductivity in FePn/Ch has much in common with that of copper oxides; in particular, the ratio of  $T_c$  versus the superfluid density is close to the Uemura plot observed for hole-doped high- $T_c$  cuprates [129,130]; as for cuprates, the electronic nematicity has been observed in the normal states of many—if not all—the FePn/Ch.

At the same time, FePn/Ch is different in many respects from cuprates. Thus, the high field inelastic neutron scattering data in the optimally doped Fe(Se,Te) superconductor [131] and in 112-type pnictide [132] show that—similar to cuprates—magnetic fluctuations play a central role in iron superconductivity; however, these suggest that the superconductivity of FePn/Ch is actually driven by a spin-triplet bound state. The spin-triplet nature of superconducting carriers in FePn/FeCh was proposed back in 2008 [35,133] and has been confirmed by several experimental facts [134–136], although experimental data are contradictory [137,138]. In this regard, let us turn our attention to one of the primary modern techniques used for determining the spin of superconducting carriers: measuring the spin susceptibility by measuring the Knight shift [89]. It is believed that spins in a triplet superconductor should be polarized in an external magnetic field, just like free spins in an ordinary metal. Thus, in such a system, one can expect that the spin susceptibility and the Knight shift should not have singularities in  $T_c$ . Spin anisotropy can suppress this for some directions but not for others. In a spin-singlet superconductor, the magnetic susceptibility vanishes at  $T \rightarrow 0$ . Thus, for a spin-singlet superconductivity, a decrease in the uniform spin susceptibility below  $T_c$  can be expected, although qualitatively, the same can occur for certain components of the triplet, although the vanishing susceptibility is often difficult to determine due to the background Van Vleck contribution. However, this technique does not take into account the complex nature of spin interactions and the spin structure of spin-triplet superconductors.

The “singlet-triplet” dilemma for superconducting carriers in the vast majority of superconductors is considered within the framework of the BCS scenario, while the model of anti-JT disproportionation in JT magnets represents a fundamentally different view of the mechanism of superconductivity, in which superconducting carriers are effective local, singlet or triplet, hole or electronic, composite bosons. Our model assumes that superconducting carriers in FePn/Ch compounds consist of  $e_g$  holes, and not of  $t_{2g}$  electrons, as predicted by the single-electron multi-orbital band model [125].

At the moment, we cannot present an unambiguous conclusion about the role of the mechanism of anti-JT disproportionation in iron-based superconductors; however, finding high- $T_c$  superconductivity in FePn/Ch compounds with the tetrahedral coordination of iron  $\text{Fe}^{2+}(3d^6)$  ions in the HS state, and the coexistence of unconventional magnetism, can be a key argument that supports the disproportionation scenario.

More surprisingly, our simple model provides convincing predictions of superconductivity and its features in different quasi-two-dimensional JT magnets, cuprates, nickelates, ruthenates, and ferropnictides/chalcogenides, differing both in the electronic structures of active centers, and in the local crystal structures. The model predicts hole-type bosonic spin-

singlet superconductivity in 2D cuprates and nickelates, spin–triplet hole superconductivity in FePn/FeCh with sufficiently high  $T_c$  in both systems, and electronic superconductivity in  $\text{Sr}_2\text{RuO}_4$  with very low  $T_c$ , in agreement with Hirsch’s ideas about the hole nature of the HTSC [139,140].

## 8. Summary

We believe that the unusual properties of a wide class of JT magnets—materials based on Jahn–Teller 3d and 4d ions with diverse crystal and electronic structures, ranging from quasi-two-dimensional unconventional superconductors (cuprates, nickelates, ferropnictides/chalcogenides, ruthenate  $\text{SrRuO}_4$ ), and manganites with localized superconductivity, to 3D ferrates ( $\text{CaSrFeO}_3$ , nickelates  $\text{RNiO}_3$ , and silver oxide  $\text{AgO}$  with unusual charge and magnetic orders—can be explained within the framework of a single scenario, which assumes their instability with respect to anti-Jahn–Teller  $d$ – $d$  disproportionation. As a result of disproportionation, the parent (“progenitor”) JT magnet is transformed into a half-filled system that is equivalent to a single- or two-band system of effective local composite spin–singlet or spin–triplet, electron or hole  $S$ -type bosons in a magnetic or non-magnetic lattice, which gives rise to an extremely rich set of phase states, from non-magnetic and magnetic insulators, unusual magnetic metallic and superconducting states, to a specific nematic ordering of the EH dimers. The effective composite bosons cannot be considered conventional quasiparticles; they are an integral part of many-electron configurations. The effective spin-dependent two-particle bosonic transport in two-band JT magnets results in behavior that is typical for “double-exchange” systems.

The model provides a comprehensive understanding of the well-established charge and magnetic order in JT ferrates and nickelates  $\text{RNiO}_3$ , including the nontrivial effect of the cation–anion–cation-bonding angle.

The most optimal conditions for HTSC with spin–singlet local composite bosons and a spinless lattice can only be achieved for low-symmetry quasi-two-dimensional  $d^9$  JT magnets, such as 2D cuprates and nickelates, where disproportionation follows the traditional Jahn–Teller effect and orbital ordering.

The anti-JT disproportionation model points to a possibility of spin–triplet superconductivity in ruthenates  $\text{Sr}_2\text{RuO}_4$  and  $\text{RuO}_2$ , ferropnictides/chalcogenides FePn/FeCh, and manganite  $\text{LaMnO}_3$ , although in most of the known “candidates” ( $\text{Ca}(\text{Sr})\text{FeO}_3$ ,  $\text{RNiO}_3$ ,  $\text{AgO}$ ), a specific spin–charge order is realized. The model assumes that effective superconducting carriers in the FePn/FeCh compounds consist of  $e_g$  holes rather than  $t_{2g}$  electrons, as predicted by the one-electron multi-orbital band models. The effective Hamiltonians for spin–triplet composite bosons in nonmagnetic and magnetic lattices have complex spin structures, which must be taken into account when interpreting experiments to determine the spin of superconducting carriers.

**Funding:** The research was supported by the Ministry of Education and Science of the Russian Federation, project No. FEUZ-2023-0017.

**Acknowledgments:** I thank Yuri Panov for the very fruitful multi-year collaboration and the stimulating and encouraging discussions.

**Conflicts of Interest:** The authors declare no conflict of interest.

## References

1. Bersuker, I. *The Jahn–Teller Effect*, 1st ed.; Cambridge University Press: Cambridge, UK; New York, NY, USA, 2006.
2. Kugel', K.I.; Khomskii, D.I. The Jahn–Teller effect and magnetism: Transition metal compounds. *Sov. Phys. Uspekhi* **1982**, *25*, 231–256. [CrossRef]
3. Sugano, S.; Tanabe, Y.; Kamimura, H. *Multiplets of Transition–Metal Ions in Crystals*; Number v. 33 in Pure and Applied Physics; Academic Press: New York, NY, USA, 1970.
4. Moskvina, A. *Atomy v Krystallakh (Atoms in Crystals)*, 1st ed.; Ural Federal University: Ekaterinburg, Russia, 2018. (In Russian)
5. Bednorz, J.G.; Müller, K.A. Possible high  $T_c$  superconductivity in the Ba–La–Cu–O system. *Z. Phys. B Condens. Matter* **1986**, *64*, 189–193. [CrossRef]

6. Ionov, S.P.; Ionova, G.V.; Lubimov, V.S.; Makarov, E.F. Instability of Crystal Lattices with Respect to Electron Density Redistributions. *Phys. Status Solidi (B)* **1975**, *71*, 11–57. [[CrossRef](#)]
7. Anderson, P.W. Model for the Electronic Structure of Amorphous Semiconductors. *Phys. Rev. Lett.* **1975**, *34*, 953–955. [[CrossRef](#)]
8. Scheurell, S.; Scholz, F.; Olesch, T.; Kemnitz, E. Electrochemical evidence for  $\text{Cu}^{3+}$ - $\text{Cu}^{2+}$ - $\text{Cu}^+$  transitions in the orthorhombic  $\text{YBa}_2\text{Cu}_3\text{O}_{7-x}$  phase. *Supercond. Sci. Technol.* **1992**, *5*, 303–305. [[CrossRef](#)]
9. Larsson, S. Mixed valence model for superconductivity. *Braz. J. Phys.* **2003**, *33*, 744–749. [[CrossRef](#)]
10. Wilson, J.A. Again ‘why layered, square-planar, mixed-valent cuprates alone?’—Further pursuit of the ‘chemical’ negative- $U$  Route HTSC Mech. *J. Phys. Condens. Matter* **2000**, *12*, R517–R547. [[CrossRef](#)]
11. Hirsch, J.E.; Scalapino, D.J. Double-valence-fluctuating molecules and superconductivity. *Phys. Rev. B* **1985**, *32*, 5639–5643. [[CrossRef](#)]
12. Sleight, A.W. Oxide Superconductors: A Chemist’s View. *MRS Proc.* **1987**, *99*, 3. [[CrossRef](#)]
13. Kulik, I.O.; Pedan, A.G. Phase transition in a model of superconducting glass. *Sov. Phys. JETP* **1980**, *52*, 742–748.
14. Rice, T.M.; Sneddon, L. Real-Space and  $\vec{k}$ -Space Electron Pairing in  $\text{BaPb}_{1-x}\text{Bi}_x\text{O}_3$ . *Phys. Rev. Lett.* **1981**, *47*, 689–692. [[CrossRef](#)]
15. David, W.I.F.; Harrison, W.T.A.; Gunn, J.M.F.; Moze, O.; Soper, A.K.; Day, P.; Jorgensen, J.D.; Hinks, D.G.; Beno, M.A.; Soderholm, L.; et al. Structure and crystal chemistry of the high- $T_c$  superconductor  $\text{YBa}_2\text{Cu}_3\text{O}_{7-x}$ . *Nature* **1987**, *327*, 310–312. [[CrossRef](#)]
16. Varma, C.M. Missing valence states, diamagnetic insulators, and superconductors. *Phys. Rev. Lett.* **1988**, *61*, 2713–2716. [[CrossRef](#)] [[PubMed](#)]
17. Dzyaloshinskii, I.E. Chemical nature of the pairing of holes in high-temperature superconductors. *JETP Lett.* **1989**, *49*, 142–144.
18. Geballe, T.; Moyzhes, B.Y. Qualitative understanding of the highest  $T_c$  cuprates. *Phys. C Supercond.* **2000**, *341–348*, 1821–1824. [[CrossRef](#)]
19. Mitsen, K.V.; Ivanenko, O.M. Phase diagram of  $\text{La}_{2-x}\text{M}_x\text{CuO}_4$  Key Underst. Nat. High-  $T_c$  Supercond. *Phys.-Uspekhi* **2004**, *47*, 493–510. [[CrossRef](#)]
20. Tsendin, K.D.; Popov, B.P.; Denisov, D.V. Explanation of the phase diagram of high-temperature superconductors in terms of the model of negative-  $U$  Centres Supercond. *Supercond. Sci. Technol.* **2006**, *19*, 313–318. [[CrossRef](#)]
21. Katayama-Yoshida, H.; Kusakabe, K.; Kizaki, H.; Nakanishi, A. General Rule and Materials Design of Negative Effective  $U$  System High-  $T_c$  Superconductivity. *Appl. Phys. Express* **2008**, *1*, 081703. [[CrossRef](#)]
22. Pouchard, M.; Villesuzanne, A. Are Superconductivity Mechanisms a Matter for Chemists? *Condens. Matter* **2020**, *5*, 67. [[CrossRef](#)]
23. Mazin, I.I.; Khomskii, D.I.; Lengsdorf, R.; Alonso, J.A.; Marshall, W.G.; Ibberson, R.M.; Podlesnyak, A.; Martínez-Lope, M.J.; Abd-Elmeguid, M.M. Charge Ordering as Alternative to Jahn-Teller Distortion. *Phys. Rev. Lett.* **2007**, *98*, 176406. [[CrossRef](#)]
24. Ogg, R.A. Bose-Einstein Condensation of Trapped Electron Pairs. Phase Separation and Superconductivity of Metal-Ammonia Solutions. *Phys. Rev.* **1946**, *69*, 243–244. [[CrossRef](#)]
25. Schafroth, M.R. Superconductivity of a Charged Ideal Bose Gas. *Phys. Rev.* **1955**, *100*, 463–475. [[CrossRef](#)]
26. Alexandrov, A.S. High-temperature superconductivity: The explanation. *Phys. Scr.* **2011**, *83*, 038301. [[CrossRef](#)]
27. Müller, K.A. The Polaronic Basis for High-Temperature Superconductivity. *J. Supercond. Nov. Magn.* **2017**, *30*, 3007–3018. [[CrossRef](#)]
28. Pavuna, D.; Dubuis, G.; Bollinger, A.T.; Wu, J.; He, X.; Božović, I. On Local Pairs vs. BCS: Quo Vadis High-  $T_c$  Superconductivity. *J. Supercond. Nov. Magn.* **2017**, *30*, 731–734. [[CrossRef](#)]
29. Božović, I.; He, X.; Wu, J.; Bollinger, A.T. Dependence of the critical temperature in overdoped copper oxides on superfluid density. *Nature* **2016**, *536*, 309–311. [[CrossRef](#)]
30. Pelc, D.; Popčević, P.; Požek, M.; Greven, M.; Barišić, N. Unusual behavior of cuprates explained by heterogeneous charge localization. *Sci. Adv.* **2019**, *5*, eaau4538. [[CrossRef](#)]
31. Moskvina, A.S. Perspectives of disproportionation driven superconductivity in strongly correlated 3d compounds. *J. Phys. Condens. Matter* **2013**, *25*, 085601. [[CrossRef](#)]
32. Allen, P.B.; Perebeinos, V. Anti-Jahn-Teller polaron in  $\text{LaMnO}_3$ . *Phys. Rev. B* **1999**, *60*, 10747–10753. [[CrossRef](#)]
33. Feng, N.; Han, J.; Lin, C.; Ai, Z.; Lan, C.; Bi, K.; Lin, Y.; Xue, K.H.; Xu, B. Anti-Jahn-Teller effect induced ultrafast insulator to metal transition in perovskite  $\text{BaBiO}_3$ . *Npj Comput. Mater.* **2022**, *8*, 226. [[CrossRef](#)]
34. Kamimura, H.; Araidai, M.; Ishida, K.; Matsuno, S.; Sakata, H.; Shiraishi, K.; Sugino, O.; Tsai, J.S. First-Principles Calculation of Copper Oxide Superconductors That Supports the Kamimura-Suwa Model. *Condens. Matter* **2020**, *5*, 69. [[CrossRef](#)]
35. Moskvina, A.S.; Avvakumov, I.L. Why does the tetrahedrally coordinated Fe drive the superconductivity? In Proceedings of the III International Conference “Fundamental Problems of High-Temperature Superconductivity”, Moscow, Zvenigorod, 13–17 October 2008; p. 215.
36. Larsson, S. Strong electron correlation and phonon coupling in high  $T_c$  superconductors. *Phys. C Supercond.* **2007**, *460–462*, 1063–1065. [[CrossRef](#)]
37. Alonso, J.A.; García-Muñoz, J.L.; Fernández-Díaz, M.T.; Aranda, M.A.G.; Martínez-Lope, M.J.; Casais, M.T. Charge Disproportionation in  $\text{R NiO}_3$  Perovskites: Simultaneous Metal-Insulator and Structural Transition in  $\text{YNiO}_3$ . *Phys. Rev. Lett.* **1999**, *82*, 3871–3874. [[CrossRef](#)]
38. Woodward, P.M.; Cox, D.E.; Moshopoulou, E.; Sleight, A.W.; Morimoto, S. Structural studies of charge disproportionation and magnetic order in  $\text{CaFeO}_3$ . *Phys. Rev. B* **2000**, *62*, 844–855. [[CrossRef](#)]
39. Uchiyama, H.; Baron, A.Q.R.; Tsutsui, S.; Tanaka, Y.; Hu, W.Z.; Yamamoto, A.; Tajima, S.; Endoh, Y. Softening of Cu-O Bond Stretching Phonons in Tetragonal  $\text{HgBa}_2\text{CuO}_4 + \delta$ . *Phys. Rev. Lett.* **2004**, *92*, 197005. [[CrossRef](#)] [[PubMed](#)]

40. Vikhnin, V.S.; Kapphan, S.E. New type charge transfer states in ferroelectric oxides: Actual problems. *Radiat. Eff. Defects Solids* **2002**, *157*, 853–856. [[CrossRef](#)]
41. Mazumdar, S. Negative charge-transfer gap and even parity superconductivity in  $\text{Sr}_2\text{RuO}_4$ . *Phys. Rev. Res.* **2020**, *2*, 023382. [[CrossRef](#)]
42. Green, R.J.; Haverkort, M.W.; Sawatzky, G.A. Bond disproportionation and dynamical charge fluctuations in the perovskite rare-earth nickelates. *Phys. Rev. B* **2016**, *94*, 195127. [[CrossRef](#)]
43. Moskvina, A.; Panov, Y. Model of charge triplets for high- $T_c$  cuprates. *J. Magn. Magn. Mater.* **2022**, *550*, 169004. [[CrossRef](#)]
44. Moskvina, A.; Panov, Y. Effective-Field Theory for Model High- $T_c$  Cuprates. *Condens. Matter* **2021**, *6*, 24. [[CrossRef](#)]
45. Moskvina, A.S. Charge transfer excitons in HTSC cuprates and nickelates. *Opt. I Spektrosk.* **2023**, *131*, 491–501. [[CrossRef](#)]
46. Zener, C. Interaction between the d -Shells in the Transition Metals. II. Ferromagnetic Compounds of Manganese with Perovskite Structure. *Phys. Rev.* **1951**, *82*, 403–405. [[CrossRef](#)]
47. Merz, M.; Nücker, N.; Schuppler, S.; Arena, D.; Dvorak, J.; Idzerda, Y.U.; Ustinovich, S.N.; Soldatov, A.G.; Shiryayev, S.V.; Barilo, S.N. X-ray absorption of  $\text{Ba}_{1-x}\text{K}_x\text{BiO}_3$   $\text{BaPb}_{1-y}\text{Bi}_y\text{O}_3$ : Competition Bipolaronic Charg-Density Wave States. *Europhys. Lett. (EPL)* **2005**, *72*, 275–281. [[CrossRef](#)]
48. Chaillout, C.; Santoro, A.; Remeika, J.; Cooper, A.; Espinosa, G.; Marezio, M. Bismuth valence order-disorder study in  $\text{BaBiO}_3$  by powder neutron diffraction. *Solid State Commun.* **1988**, *65*, 1363–1369. [[CrossRef](#)]
49. Rodríguez-Carvajal, J.; Hennion, M.; Moussa, F.; Moudden, A.H.; Pinsard, L.; Revolevschi, A. Neutron-diffraction study of the Jahn-Teller transition in stoichiometric  $\text{LaMnO}_3$ . *Phys. Rev. B* **1998**, *57*, R3189–R3192. [[CrossRef](#)]
50. Huang, Q.; Santoro, A.; Lynn, J.W.; Erwin, R.W.; Borchers, J.A.; Peng, J.L.; Greene, R.L. Structure and magnetic order in undoped lanthanum manganite. *Phys. Rev. B* **1997**, *55*, 14987–14999. [[CrossRef](#)]
51. Moskvina, A.S. Disproportionation and electronic phase separation in parent manganite  $\text{LaMnO}_3$ . *Phys. Rev. B* **2009**, *79*, 115102. [[CrossRef](#)]
52. Moskvina, A.S.; Ovanesyan, N.S.; Trukhtanov, V.A. Angular dependence of the superexchange interaction  $\text{Fe}^{3+}\text{-O}^{2-}\text{-Cr}^{3+}$ . *Hyperfine Interact.* **1975**, *1*, 265–281. [[CrossRef](#)]
53. Moskvina, A.S. Dzyaloshinskii Interaction and Exchange-Relativistic Effects in Orthoferrites. *J. Exp. Theor. Phys.* **2021**, *132*, 517–547. [[CrossRef](#)]
54. Moskvina, A. Structure–Property Relationships for Weak Ferromagnetic Perovskites. *Magnetochemistry* **2021**, *7*, 111. [[CrossRef](#)]
55. Alonso, J.A.; Martínez-Lope, M.J.; Casais, M.T.; Fernández-Díaz, M.T. Evolution of the Jahn-Teller Distortion of  $\text{MnO}_6$  Octahedra in  $\text{RMnO}_3$  Perovskites ( $R = \text{Pr, Nd, Dy, Tb, Ho, Er, Y}$ ): A Neutron Diffraction Study. *Inorg. Chem.* **2000**, *39*, 917–923. [[CrossRef](#)]
56. Pangburn, E.; Banerjee, A.; Freire, H.; Pépin, C. Incoherent transport in a model for the strange metal phase: Memory-matrix formalism. *Phys. Rev. B* **2023**, *107*, 245109. [[CrossRef](#)]
57. Moskvina, A.S.; Panov, Y.D. Nature of the Pseudogap Phase of HTSC Cuprates. *Phys. Solid State* **2020**, *62*, 1554–1561. [[CrossRef](#)]
58. Moskvina, A.S.; Panov, Y.D. Phase separation in high- $T_c$  cuprates. *J. Phys. Conf. Ser.* **2022**, *2164*, 012014. [[CrossRef](#)]
59. Gong, W.; Greedan, J.; Liu, G.; Bjorgvinsson, M. Crystal structure and magnetic properties of orthorhombic  $\text{Sr}_2\text{VO}_4$  with tetrahedral vanadium (IV). *J. Solid State Chem.* **1991**, *95*, 213–219. [[CrossRef](#)]
60. Deisenhofer, J.; Schaile, S.; Teyssier, J.; Wang, Z.; Hemmida, M.; Von Nidda, H.A.K.; Eremina, R.M.; Eremin, M.V.; Viennois, R.; Giannini, E.; et al. Electron spin resonance and exchange paths in the orthorhombic dimer system  $\text{Sr}_2\text{VO}_4$ . *Phys. Rev. B* **2012**, *86*, 214417. [[CrossRef](#)]
61. Wang, Z.; Kamenskiy, D.; Cépas, O.; Schmidt, M.; Quintero-Castro, D.L.; Islam, A.T.M.N.; Lake, B.; Aczel, A.A.; Dabkowska, H.A.; Dabkowski, A.B.; et al. High-field electron spin resonance spectroscopy of singlet-triplet transitions in the spin-dimer systems  $\text{Sr}_3\text{Cr}_2\text{O}_8$  and  $\text{Ba}_3\text{Cr}_2\text{O}_8$ . *Phys. Rev. B* **2014**, *89*, 174406. [[CrossRef](#)]
62. Barone, P.; Yamauchi, K.; Picozzi, S. Jahn-Teller distortions as a novel source of multiferroicity. *Phys. Rev. B* **2015**, *92*, 014116. [[CrossRef](#)]
63. Hepting, M. The Rare-Earth Nickelates. In *Ordering Phenomena in Rare-Earth Nickelate Heterostructures*; Series Title: Springer Theses; Springer International Publishing: Cham, Switzerland, 2017; pp. 13–29. [[CrossRef](#)]
64. Chaloupka, J.; Khaliullin, G. Orbital Order and Possible Superconductivity in  $\text{LaNiO}_3/\text{LaMO}_3$  Superlattices. *Phys. Rev. Lett.* **2008**, *100*, 016404. [[CrossRef](#)]
65. Gawryluk, D.J.; Klein, Y.M.; Shang, T.; Sheptyakov, D.; Keller, L.; Casati, N.; Lacorre, P.; Fernández-Díaz, M.T.; Rodríguez-Carvajal, J.; Medarde, M. Distortion mode anomalies in bulk  $\text{PrNiO}_3$ : Illustrating the potential of symmetry-adapted distortion mode analysis for the study of phase transitions. *Phys. Rev. B* **2019**, *100*, 205137. [[CrossRef](#)]
66. Kumar, D.; Rajeev, K.P.; Alonso, J.A.; Martínez-Lope, M.J. Spin-canted magnetism and decoupling of charge and spin ordering in  $\text{NdNiO}_3$ . *Phys. Rev. B* **2013**, *88*, 014410. [[CrossRef](#)]
67. Bousquet, E.; Cano, A. Non-collinear magnetism & multiferroicity: The perovskite case. *Phys. Sci. Rev.* **2023**, *8*, 479–508. [[CrossRef](#)]
68. Zhang, J.; Zheng, H.; Ren, Y.; Mitchell, J.F. High-Pressure Floating-Zone Growth of Perovskite Nickelate  $\text{LaNiO}_3$  Single Crystals. *Cryst. Growth Des.* **2017**, *17*, 2730–2735. [[CrossRef](#)]
69. Guo, H.; Li, Z.W.; Zhao, L.; Hu, Z.; Chang, C.F.; Kuo, C.Y.; Schmidt, W.; Piovano, A.; Pi, T.W.; Sobolev, O.; et al. Antiferromagnetic correlations in the metallic strongly correlated transition metal oxide  $\text{LaNiO}_3$ . *Nat. Commun.* **2018**, *9*, 43. [[CrossRef](#)] [[PubMed](#)]

70. Shamblin, J.; Heres, M.; Zhou, H.; Sangoro, J.; Lang, M.; Neufeind, J.; Alonso, J.A.; Johnston, S. Experimental evidence for bipolaron condensation as a mechanism for the metal–insulator transition in rare-earth nickelates. *Nat. Commun.* **2018**, *9*, 86. [[CrossRef](#)] [[PubMed](#)]
71. Li, B.; Louca, D.; Yano, S.; Marshall, L.G.; Zhou, J.; Goodenough, J.B. Insulating Pockets in Metallic LaNiO<sub>3</sub>. *Adv. Electron. Mater.* **2016**, *2*, 1500261. [[CrossRef](#)]
72. Wawrzyńska, E.; Coldea, R.; Wheeler, E.M.; Mazin, I.I.; Johannes, M.D.; Sörgel, T.; Jansen, M.; Ibberson, R.M.; Radaelli, P.G. Orbital Degeneracy Removed by Charge Order in Triangular Antiferromagnet AgNiO<sub>2</sub>. *Phys. Rev. Lett.* **2007**, *99*, 157204. [[CrossRef](#)]
73. Chen, H.; Freeman, C.L.; Harding, J.H. Charge disproportionation and Jahn-Teller distortion in LiNiO<sub>2</sub> and NaNiO<sub>2</sub>: A density functional theory study. *Phys. Rev. B* **2011**, *84*, 085108. [[CrossRef](#)]
74. Zhang, F.C.; Rice, T.M. Effective Hamiltonian for the superconducting Cu oxides. *Phys. Rev. B* **1988**, *37*, 3759–3761. [[CrossRef](#)]
75. Moskvin, A.S. True charge-transfer gap in parent insulating cuprates. *Phys. Rev. B* **2011**, *84*, 075116. [[CrossRef](#)]
76. Moskvin, A.S.; Panov, Y.D. Topological Structures in Unconventional Scenario for 2D Cuprates. *J. Supercond. Nov. Magn.* **2019**, *32*, 61–84. [[CrossRef](#)]
77. Moskvin, A.S.; Panov, Y.D. Electron–Hole Dimers in the Parent Phase of Quasi–2D Cuprates. *Phys. Solid State* **2019**, *61*, 1553–1558. [[CrossRef](#)]
78. Moskvin, A.S. Large Variety of the On-Site Order Parameters and Phase States in Quasi-2D HTSC Cuprates. *Phys. Met. Metallogr.* **2019**, *120*, 1252–1259. [[CrossRef](#)]
79. Naito, M.; Krockenberger, Y.; Ikeda, A.; Yamamoto, H. Reassessment of the electronic state, magnetism, and superconductivity in high-T<sub>c</sub> cuprates with the Nd<sub>2</sub>CuO<sub>4</sub> structure. *Phys. C Supercond. Its Appl.* **2016**, *523*, 28–54. [[CrossRef](#)]
80. Li, D.; Lee, K.; Wang, B.Y.; Osada, M.; Crossley, S.; Lee, H.R.; Cui, Y.; Hikita, Y.; Hwang, H.Y. Superconductivity in an infinite-layer nickelate. *Nature* **2019**, *572*, 624–627. [[CrossRef](#)]
81. Panov, Y.D. Critical Temperatures of a Model Cuprate. *Phys. Met. Metallogr.* **2019**, *120*, 1276–1281. [[CrossRef](#)]
82. Fischer, P.; Roult, G.; Schwarzenbach, D. Crystal and magnetic structure of silver difluoride-II. Weak 4d-ferromagnetism of AgF<sub>2</sub>. *J. Phys. Chem. Solids* **1971**, *32*, 1641–1647. [[CrossRef](#)]
83. Derzsi, M.; Tokár, K.; Piekarczyk, P.; Grochala, W. Charge ordering mechanism in silver difluoride. *Phys. Rev. B* **2022**, *105*, L081113. [[CrossRef](#)]
84. Bachar, N.; Koterak, K.; Gawraczynski, J.; Trzciński, W.; Paszula, J.; Piombo, R.; Barone, P.; Mazej, Z.; Ghiringhelli, G.; Nag, A.; et al. Charge-Transfer and d d excitations in AgF<sub>2</sub>. *Phys. Rev. Res.* **2022**, *4*, 023108. [[CrossRef](#)]
85. Shen, C.; Žemva, B.; Lucier, G.M.; Graudejus, O.; Allman, J.A.; Bartlett, N. Disproportionation of Ag(II) to Ag(I) and Ag(III) in Fluoride Systems and Syntheses and Structures of (AgF<sup>+</sup>)<sub>2</sub> AgF<sub>4</sub><sup>−</sup> MF<sub>6</sub><sup>−</sup> Salts (M = As, Sb, Pt, Au, Ru). *Inorg. Chem.* **1999**, *38*, 4570–4577. [[CrossRef](#)]
86. Tokár, K.; Derzsi, M.; Grochala, W. Comparative computational study of antiferromagnetic and mixed-valent diamagnetic phase of AgF<sub>2</sub>: Crystal, electronic and phonon structure and p-T phase diagram. *Comput. Mater. Sci.* **2021**, *188*, 110250. [[CrossRef](#)]
87. Scatturin, V.; Bellon, P.L.; Salkind, A.J. The Structure of Silver Oxide Determined by Means of Neutron Diffraction. *J. Electrochem. Soc.* **1961**, *108*, 819. [[CrossRef](#)]
88. Allen, J.P.; Scanlon, D.O.; Watson, G.W. Electronic structures of silver oxides. *Phys. Rev. B* **2011**, *84*, 115141. [[CrossRef](#)]
89. Hirschfeld, P.J. Using gap symmetry and structure to reveal the pairing mechanism in Fe-based superconductors. *Comptes Rendus Phys.* **2016**, *17*, 197–231. [[CrossRef](#)]
90. Dong, S.; Yu, R.; Yunoki, S.; Liu, J.M.; Dagotto, E. Double-exchange model study of multiferroic RMnO<sub>3</sub> perovskites. *Eur. Phys. J. B* **2009**, *71*, 339–344. [[CrossRef](#)]
91. Stout, J.W.; DeLassus, P.; Graham, C.D.; Rhyne, J.J. CrF<sub>2</sub>, A Canted Antiferromagnet. *AIP Conf. Proc.* **1972**, *5*, 669. [[CrossRef](#)]
92. Jiménez-Mier, J.; Olalde-Velasco, P.; Yang, W.L.; Denlinger, J. X-ray absorption and resonant inelastic x-ray scattering (RIXS) show the presence of Cr<sup>+</sup> at the surface and in the bulk of CrF<sub>2</sub>. In Proceedings of the AIP Conference Proceedings, Ciudad Juárez, Mexico, 4–6 March 2015; p. 020002. [[CrossRef](#)]
93. Raffaele, R.; Anderson, H.U.; Sparlin, D.M.; Parris, P.E. Transport anomalies in the high-temperature hopping conductivity and thermopower of Sr-doped La(Cr,Mn)O<sub>3</sub>. *Phys. Rev. B* **1991**, *43*, 7991–7999. [[CrossRef](#)]
94. Van Roosmalen, J.; Cordfunke, E. The Defect Chemistry of LaMnO<sub>3±δ</sub>. *J. Solid State Chem.* **1994**, *110*, 109–112. [[CrossRef](#)]
95. Zhou, J.S.; Goodenough, J.B. Paramagnetic phase in single-crystal LaMnO<sub>3</sub>. *Phys. Rev. B* **1999**, *60*, R15002–R15004. [[CrossRef](#)]
96. Ritter, C.; Ibarra, M.R.; De Teresa, J.M.; Algarabel, P.A.; Marquina, C.; Blasco, J.; García, J.; Oseroff, S.; Cheong, S.W. Influence of oxygen content on the structural, magnetotransport, and magnetic properties of LaMnO<sub>3±δ</sub>. *Phys. Rev. B* **1997**, *56*, 8902–8911. [[CrossRef](#)]
97. Kim, Y.J. p-Wave Pairing and Colossal Magnetoresistance in Manganese Oxides. *Mod. Phys. Lett. B* **1998**, *12*, 507–518. [[CrossRef](#)]
98. Krivoruchko, V.N. Local spin-triplet superconductivity in half-metallic manganites: A perspective platform for high-temperature topological superconductivity. *Low Temp. Phys.* **2021**, *47*, 901–907. [[CrossRef](#)]
99. Markovich, V.; Fita, I.; Wisniewski, A.; Puzniak, R.; Mogilyansky, D.; Titelman, L.; Vladman, L.; Herskowitz, M.; Gorodetsky, G. Metastable diamagnetic response of 20 nm La<sub>1−x</sub>MnO<sub>3</sub> particles. *Phys. Rev. B* **2008**, *77*, 014423. [[CrossRef](#)]
100. Kasai, M.; Ohno, T.; Kanke, Y.; Kozono, Y.; Hanazono, M.; Sugita, Y. Current-Voltage Characteristics of YBa<sub>2</sub>Cu<sub>3</sub>O<sub>y</sub>/La<sub>0.7</sub>Ca<sub>0.3</sub>MnO<sub>z</sub>/YBa<sub>2</sub>Cu<sub>3</sub>O<sub>y</sub> Trilayered-Type Junctions. *Jpn. J. Appl. Phys.* **1990**, *29*, L2219. [[CrossRef](#)]

101. Mitin, A.; Kuz'micheva, G.; Novikova, S. Mixed Oxides of Manganese with Perovskite and Perovskite-related Structures. *Russ. J. Inorg. Chem.* **1997**, *42*, 1791. [[CrossRef](#)]
102. Nath, R.; Raychaudhuri, A.K.; Mukovskii, Y.M.; Mondal, P.; Bhattacharya, D.; Mandal, P. Electric field driven destabilization of the insulating state in nominally pure LaMnO<sub>3</sub>. *J. Phys. Condens. Matter* **2013**, *25*, 155605. [[CrossRef](#)]
103. Cabassi, R.; Bolzoni, F.; Gilioli, E.; Bissoli, F.; Prodi, A.; Gauzzi, A. Jahn-Teller-induced crossover of the paramagnetic response in the singly valent  $e_g$  system LaMn<sub>7</sub>O<sub>12</sub>. *Phys. Rev. B* **2010**, *81*, 214412. [[CrossRef](#)]
104. Schaile, S.; Von Nidda, H.A.K.; Deisenhofer, J.; Loidl, A.; Nakajima, T.; Ueda, Y. Korringa-like relaxation in the high-temperature phase of A-site ordered YBaMn<sub>2</sub>O<sub>6</sub>. *Phys. Rev. B* **2012**, *85*, 205121. [[CrossRef](#)]
105. Takano, M.; Nakanishi, N.; Takeda, Y.; Naka, S.; Takada, T. Charge disproportionation in CaFeO<sub>3</sub> studied with the Mössbauer effect. *Mater. Res. Bull.* **1977**, *12*, 923–928. [[CrossRef](#)]
106. Takeda, T.; Kanno, R.; Kawamoto, Y.; Takano, M.; Kawasaki, S.; Kamiyama, T.; Izumi, F. Metal–semiconductor transition, charge disproportionation, and low-temperature structure of Ca<sub>1-x</sub>Sr<sub>x</sub>FeO<sub>3</sub> synthesized under high-oxygen pressure. *Solid State Sci.* **2000**, *2*, 673–687. [[CrossRef](#)]
107. Reehuis, M.; Ulrich, C.; Maljuk, A.; Niedermayer, C.; Ouladdiaf, B.; Hoser, A.; Hofmann, T.; Keimer, B. Neutron diffraction study of spin and charge ordering in SrFeO<sub>3-δ</sub>. *Phys. Rev. B* **2012**, *85*, 184109. [[CrossRef](#)]
108. Chakraverty, S.; Matsuda, T.; Ogawa, N.; Wadati, H.; Ikenaga, E.; Kawasaki, M.; Tokura, Y.; Hwang, H.Y. BaFeO<sub>3</sub> cubic single crystalline thin film: A ferromagnetic insulator. *Appl. Phys. Lett.* **2013**, *103*, 142416. [[CrossRef](#)]
109. Fujioka, J.; Ishiwata, S.; Kaneko, Y.; Taguchi, Y.; Tokura, Y. Variation of charge dynamics upon the helimagnetic and metal–insulator transitions for perovskite AFeO<sub>3</sub> (A = Sr and Ca). *Phys. Rev. B* **2012**, *85*, 155141. [[CrossRef](#)]
110. Kuzushita, K.; Morimoto, S.; Nasu, S.; Nakamura, S. Charge Disproportionation and Antiferromagnetic Order of Sr<sub>3</sub>Fe<sub>2</sub>O<sub>7</sub>. *J. Phys. Soc. Jpn.* **2000**, *69*, 2767–2770. [[CrossRef](#)]
111. Kim, J.H.; Peets, D.C.; Reehuis, M.; Adler, P.; Maljuk, A.; Ritschel, T.; Allison, M.C.; Geck, J.; Mardegan, J.R.L.; Bereciartua Perez, P.J.; et al. Hidden Charge Order in an Iron Oxide Square-Lattice Compound. *Phys. Rev. Lett.* **2021**, *127*, 097203. [[CrossRef](#)]
112. Adler, P. Properties of K<sub>2</sub>NiF<sub>4</sub>-Type Oxides Sr<sub>2</sub>FeO<sub>4</sub>. *J. Solid State Chem.* **1994**, *108*, 275–283. [[CrossRef](#)]
113. Adler, P.; Reehuis, M.; Stüßler, N.; Medvedev, S.A.; Nicklas, M.; Peets, D.C.; Bertinshaw, J.; Christensen, C.K.; Etter, M.; Hoser, A.; et al. Spiral magnetism, spin flop, and pressure-induced ferromagnetism in the negative charge-transfer-gap insulator Sr<sub>2</sub>FeO<sub>4</sub>. *Phys. Rev. B* **2022**, *105*, 054417. [[CrossRef](#)]
114. Itoh, M.; Shikano, M.; Shimura, T. High- and low-spin transition of Ru<sup>4+</sup> in the perovskite-related layered system Sr<sub>n+1</sub>Ru<sub>n</sub>O<sub>3n+1</sub> (N = 1, 2, ∞) Change n. *Phys. Rev. B* **1995**, *51*, 16432–16435. [[CrossRef](#)]
115. Grutter, A.J.; Wong, F.J.; Arenholz, E.; Vailionis, A.; Suzuki, Y. Evidence of high-spin Ru and universal magnetic anisotropy in SrRuO<sub>3</sub> thin films. *Phys. Rev. B* **2012**, *85*, 134429. [[CrossRef](#)]
116. Cao, G.; Song, W.; Sun, Y.; Lin, X. Violation of the Mott–Ioffe–Regel limit: High-temperature resistivity of itinerant magnets Sr<sub>n+1</sub>Ru<sub>n</sub>O<sub>3n+1</sub> (n = 2, 3, ∞) and CaRuO<sub>3</sub>. *Solid State Commun.* **2004**, *131*, 331–336. [[CrossRef](#)]
117. Nakatsuji, S.; Maeno, Y. Quasi-Two-Dimensional Mott Transition System Ca<sub>2-x</sub>Sr<sub>x</sub>RuO<sub>4</sub>. *Phys. Rev. Lett.* **2000**, *84*, 2666–2669. [[CrossRef](#)] [[PubMed](#)]
118. Nobukane, H.; Yanagihara, K.; Kunisada, Y.; Ogasawara, Y.; Isono, K.; Nomura, K.; Tanahashi, K.; Nomura, T.; Akiyama, T.; Tanda, S. Co-appearance of superconductivity and ferromagnetism in a Ca<sub>2</sub>RuO<sub>4</sub> nanofilm crystal. *Sci. Rep.* **2020**, *10*, 3462. [[CrossRef](#)] [[PubMed](#)]
119. Maeno, Y.; Hashimoto, H.; Yoshida, K.; Nishizaki, S.; Fujita, T.; Bednorz, J.G.; Lichtenberg, F. Superconductivity in a layered perovskite without copper. *Nature* **1994**, *372*, 532–534. [[CrossRef](#)]
120. Mackenzie, A.P.; Maeno, Y. The superconductivity of Sr<sub>2</sub>RuO<sub>4</sub> and the physics of spin-triplet pairing. *Rev. Mod. Phys.* **2003**, *75*, 657–712. [[CrossRef](#)]
121. Mackenzie, A.P.; Scaffidi, T.; Hicks, C.W.; Maeno, Y. Even odder after twenty-three years: The superconducting order parameter puzzle of Sr<sub>2</sub>RuO<sub>4</sub>. *Npj Quantum Mater.* **2017**, *2*, 40. [[CrossRef](#)]
122. Leggett, A.J.; Liu, Y. Symmetry Properties of Superconducting Order Parameter in Sr<sub>2</sub>RuO<sub>4</sub>: A Brief Review. *J. Supercond. Nov. Magn.* **2021**, *34*, 1647–1673. [[CrossRef](#)]
123. Ruf, J.P.; Paik, H.; Schreiber, N.J.; Nair, H.P.; Miao, L.; Kawasaki, J.K.; Nelson, J.N.; Faeth, B.D.; Lee, Y.; Goodge, B.H.; et al. Strain-stabilized superconductivity. *Nat. Commun.* **2021**, *12*, 59. [[CrossRef](#)]
124. Uchida, M.; Nomoto, T.; Musashi, M.; Arita, R.; Kawasaki, M. Superconductivity in Uniquely Strained RuO<sub>2</sub> Films. *Phys. Rev. Lett.* **2020**, *125*, 147001. [[CrossRef](#)]
125. Stewart, G.R. Superconductivity in iron compounds. *Rev. Mod. Phys.* **2011**, *83*, 1589–1652. [[CrossRef](#)]
126. Chubukov, A.; Hirschfeld, P.J. Iron-based superconductors, seven years later. *Phys. Today* **2015**, *68*, 46–52. [[CrossRef](#)]
127. Si, Q.; Yu, R.; Abrahams, E. High-temperature superconductivity in iron pnictides and chalcogenides. *Nat. Rev. Mater.* **2016**, *1*, 16017. [[CrossRef](#)]
128. Kreisel, A.; Hirschfeld, P.; Andersen, B. On the Remarkable Superconductivity of FeSe and Its Close Cousins. *Symmetry* **2020**, *12*, 1402. [[CrossRef](#)]

129. Carlo, J.P.; Uemura, Y.J.; Goko, T.; MacDougall, G.J.; Rodriguez, J.A.; Yu, W.; Luke, G.M.; Dai, P.; Shannon, N.; Miyasaka, S.; et al. Static Magnetic Order and Superfluid Density of R FeAs ( O , F ) ( R = La , Nd , Ce ) and LaFePO Studied by Muon Spin Relaxation: Unusual Similarities with the Behavior of Cuprate Superconductors. *Phys. Rev. Lett.* **2009**, *102*, 087001. [[CrossRef](#)] [[PubMed](#)]
130. Adamski, A.; Krellner, C.; Abdel-Hafiez, M. Signature of multigap nodeless superconductivity in fluorine-doped NdFeAsO. *Phys. Rev. B* **2017**, *96*, 100503. [[CrossRef](#)]
131. Liu, J.; Savici, A.T.; Granroth, G.E.; Habicht, K.; Qiu, Y.; Hu, J.; Mao, Z.Q.; Bao, W. A Triplet Resonance in Superconducting Fe<sub>1.03</sub>Se<sub>0.4</sub>Te<sub>0.6</sub>. *Chin. Phys. Lett.* **2018**, *35*, 127401. [[CrossRef](#)]
132. Xie, T.; Gong, D.; Ghosh, H.; Ghosh, A.; Soda, M.; Masuda, T.; Itoh, S.; Bourdarot, F.; Regnault, L.P.; Danilkin, S.; et al. Neutron Spin Resonance in the 112-Type Iron-Based Superconductor. *Phys. Rev. Lett.* **2018**, *120*, 137001. [[CrossRef](#)]
133. Lee, P.A.; Wen, X.G. Spin-triplet p -wave pairing in a three-orbital model for iron pnictide superconductors. *Phys. Rev. B* **2008**, *78*, 144517. [[CrossRef](#)]
134. Baek, S.H.; Grafe, H.J.; Hammerath, F.; Fuchs, M.; Rudisch, C.; Harnagea, L.; Aswartham, S.; Wurmehl, S.; Van Den Brink, J.; Büchner, B. <sup>75</sup>As NMR-NQR study in superconducting LiFeAs. *Eur. Phys. J. B* **2012**, *85*, 159. [[CrossRef](#)]
135. Hänke, T.; Sykora, S.; Schlegel, R.; Baumann, D.; Harnagea, L.; Wurmehl, S.; Daghofer, M.; Büchner, B.; van den Brink, J.; Hess, C. Probing the Unconventional Superconducting State of LiFeAs by Quasiparticle Interference. *Phys. Rev. Lett.* **2012**, *108*, 127001. [[CrossRef](#)]
136. Brydon, P.M.R.; Daghofer, M.; Timm, C.; Van Den Brink, J. Theory of magnetism and triplet superconductivity in LiFeAs. *Phys. Rev. B* **2011**, *83*, 060501. [[CrossRef](#)]
137. Brand, J.; Stunault, A.; Wurmehl, S.; Harnagea, L.; Büchner, B.; Meven, M.; Braden, M. Spin susceptibility in superconducting LiFeAs studied by polarized neutron diffraction. *Phys. Rev. B* **2014**, *89*, 045141. [[CrossRef](#)]
138. Gifford, J.A.; Chen, B.B.; Zhang, J.; Zhao, G.J.; Kim, D.R.; Li, B.C.; Wu, D.; Chen, T.Y. Determination of spin polarization using an unconventional iron superconductor. *AIP Adv.* **2016**, *6*, 115023. [[CrossRef](#)]
139. Hirsch, J.E. Why only hole conductors can be superconductors. In Proceedings of the Oxide-Based Materials and Devices VIII, San Francisco, CA, USA, 29 January–1 February 2017; p. 101051V. [[CrossRef](#)]
140. Hirsch, J.; Marsiglio, F. Understanding electron-doped cuprate superconductors as hole superconductors. *Phys. C Supercond. Its Appl.* **2019**, *564*, 29–37. [[CrossRef](#)]

**Disclaimer/Publisher’s Note:** The statements, opinions and data contained in all publications are solely those of the individual author(s) and contributor(s) and not of MDPI and/or the editor(s). MDPI and/or the editor(s) disclaim responsibility for any injury to people or property resulting from any ideas, methods, instructions or products referred to in the content.